Available online at www.sciencedirect.com
ScienceDirect
Progress in Oceanography 76 (2008) 334–365
Progress in Oceanography
www.elsevier.com/locate/pocean

Eddy-resolving ocean circulation in the Asian–Australian region inferred from an ocean reanalysis effort

A. Schiller [a,*], P.R. Oke [a], G. Brassington [b], M. Entel [b], R. Fiedler [a], D.A. Griffin [a], J.V. Mansbridge [a]

[a] *CSIRO Marine and Atmospheric Research, Wealth from Oceans Flagship Program, Centre for Australian Weather and Climate Research, Hobart, Tasmania, Australia*

[b] *Bureau of Meteorology, Centre for Australian Weather and Climate Research, Melbourne, Victoria, Australia*

Available online 18 January 2008

Abstract

The first global ocean reanalysis with focus on the Asian–Australian region was performed for the period October 1992 to June 2006. The 14-year experiment assimilated available observations of altimetric sea-level anomaly, satellite SST and quality-controlled *in situ* temperature and salinity profiles from a range of sources, including field surveys and the Argo float array. This study focuses on dominant circulation patterns in the South-East Asian/Australian region as simulated by an eddy-resolving and data-assimilating ocean general circulation model. New estimates of the ocean circulation are provided which are largely in agreement with the limited number of observations. Transports of key currents in the region are as follows: The total (top-to-bottom) annual mean Indonesian Throughflow transport and its standard deviation are 9.7 ± 4.4 Sv from the Pacific to the Indian Ocean with a minimum in January (6.6 Sv) and a maximum in April (12.3 Sv). The Leeuwin Current along the west coast of Australia is dominated by eddy structures with a mean southward transport of 4.1 ± 2.0 Sv at 34°S. Along the southern coast of Australia a narrow shelf edge current known as the South Australian Current advects 4.5 ± 2.6 Sv eastward at 130°E. The South Australian Current converges east of Tasmania with the eddy-rich extension of East Australian Current. At 32°S this current transports 36.8 ± 18.5 Sv southward. A dominating feature of the circulation between north-eastern Australia and Papua–New Guinea is the strong and quasi-permanent Coral Sea Gyre. This gyre is associated with the highly variable Hiri Current which runs along the south coast of Papua–New Guinea and advects 8.2 ± 19.1 Sv into the Western Pacific Ocean. All of these transport estimates are subject to strong eddy variability.

1. Introduction

Over the last decade there have been tremendous advances in ocean observing systems, particularly in remotely sensed and *in situ* ocean observing platforms (Roemmich et al., 2001). Autonomous Argo profiling floats, whose total numbers recently reached the target of 3000 (http://www.argo.net/) are now the dominant

* Corresponding author. Tel.: +61 3 6232 5300; fax: +61 3 6232 5123.
E-mail address: Andreas.Schiller@csiro.au (A. Schiller).

0079-6611/$ - see front matter
doi:10.1016/j.pocean.2008.01.003

source of sub-surface ocean information. Furthermore, supercomputers allow for the assimilation of vast amounts of observational data into large-scale eddy-resolving models, providing us with an unprecedented wealth of information about the oceans (Koblinsky and Smith, 2001).

The focus of this study is on providing an integral view of the ocean dynamics in the Asian–Australian region based on an advanced ocean reanalysis system. The Bluelink Ocean ReANalyis (BRAN) forms part of a global ocean short-range forecasting system which is run in operational mode (http://www.bom.gov.au/oceanography/projects/BLUElink/index.html). Operational oceanography and particularly numerical ocean prediction at eddy-resolving scales is still in its infancy when compared to experiences gained over many decades with Numerical Weather Prediction schemes. Furthermore, operational eddy-resolving ocean simulations with data assimilation still have to rely on the use of comparably simple assimilation and initialization techniques to reduce computational costs and achieve feasibility in operational environments (Chassignet and Verron, 2006; Schiller and Smith, 2006). On the other hand model – data fusion consistent with ocean dynamics and conservation properties is still based on computationally cheap coarse-resolution models (order 1°) and currently suffers from unrealistic representation of eddy fields and boundary currents (e.g., Stammer et al., 2003).

Since the seminal work by Semtner and Chervin (1992) on the simulation of the ocean general circulation using a global eddy-resolving model with 0.5° horizontal resolution, progress in simulating and understanding eddy-scale features in ocean dynamics has been significant. Since those early days of high-resolution Ocean General Circulation Models (OGCMs) a lot of progress has been made to improve the dynamics and sub-grid-scale parameterizations in these models (e.g., Haidvogel and Beckmann, 1999; Griffies, 2004). Here, we use such a state-of-the-art global OGCM based on GFDL's MOM code (Griffies et al., 2004) plus an advanced data assimilation scheme (Oke et al., 2005). We focus on the eddy-resolving sub-domain of the model in the South-East Asian region. This is an area with complex topography and circulation features which are not well known quantitatively. By combining model dynamics with observations this study aims to provide a comprehensive overview and estimates of flow rates of the major currents in this region.

With regard to observations we have tried to assimilate all available remotely sensed and *in situ* observations in the region to constrain our prognostic variables. As a result, the reanalysis should have produced a coherent and consistent picture of the circulation in the southeast Asian–Australian region which is in close agreement with observations.

This paper is structured as follows. In Section 2 we describe the reanalysis system, including the model, the data assimilation technique, the surface forcing and the observations assimilated into the model. Section 3 begins with an overview of the large-scale circulation in the South-East Asian/Australian region, followed by details about the circulation and transports in subdomains of the regions with focus on the Indonesian Throughflow, the Leeuwin Current, the South Australian Current and the larger East Australian Current systems. The study concludes with a discussion of the achievements and shortcomings of the reanalysis.

2. Description of the reanalysis system

The global model used here is based on version 4.0 of the Modular Ocean Model (Griffies et al., 2004), called the Ocean Forecasting Australia Model (OFAM), with a resolution grading from 2° in the North Atlantic to 1/10° in the Asian–Australian region from 90°E to 180°E, and from 16°N to 75°S. There are 47 levels in the vertical, 35 of which are in the top 1000 m, with 10 m resolution near the surface. The horizontal grid has 1191 and 968 points in the zonal and meridional directions, respectively. The bottom topography for OFAM is a composite of a range of different sources. The underlying bathymetry used is the dbdb2 product which was provided by the U.S. Naval Research Laboratories (http://www7320.nrlssc.navy.mil/DBDB2WWW), and is augmented by other bathymetries (mostly GEBCO; http://www.ngdc.noaa.gov/mgg/gebco/) to reduce errors in individual bathymetric data sets. The model uses the third-order quicker scheme for tracer advection (Leonard, 1979). Horizontal viscosity is resolution and state-dependent based on the Smagorinsky-scheme (Griffies and Hallberg, 2000). Due to the model's variable grid size anistropic options have been chosen for this parameterization. Local enhancements to the model include a hybrid mixed-layer model (Chen et al., 1994; Power et al., 2005; Schiller and Godfrey, 2003).

The model was forced by 6-hourly atmospheric fields from the 40 year reanalysis ERA-40 of the ECMWF (http://data.ecmwf.int/data/d/era40daily; Kallberg et al., 2004), which included all surface forcing fields, i.e.

wind stresses, heat and freshwater fluxes. The ERA-40 data set ends in 2002 so we used output from the operational forecasts of ECMWF for the period January 2002 to June 2006. The main difference between these two atmospheric data sets lies in their spatial resolution: 2.5° in ERA-40 and 0.5° in the operational product. The total period covered by the ocean reanalysis ranges from October 1992 to June 2006.

The thermohaline surface boundary conditions are formulated as follows. The net surface heat flux Q_{surf} is the sum of the four heat flux components provided by the ECMWF data sets:

$$Q_{\mathrm{surf}} = Q_{\mathrm{sw}} - Q_{\mathrm{sens}} - Q_{\mathrm{lat}} - Q_{\mathrm{lw}} \tag{1}$$

The boundary condition for fluxes resulting from evaporation and precipitation was formulated as the sum of a flux term (from the ECMWF data) plus restoring to monthly mean Levitus surface salinity (Levitus, 2001) with a restoring time constant of $\gamma = 30$ days.

$$(E-P) = (E-P)_{\mathrm{surf}} + (z1/SSS_{\mathrm{model}}) * (SSS_{\mathrm{obs}} - SSS_{\mathrm{model}})/\gamma. \tag{2}$$

OFAM was initialized with a blend of climatologies from CARS2000 (CSIRO Atlas of Regional Seas; Ridgway et al., 2002) and from Levitus (2001) for regions outside the Asian–Australian domain. The model integration started from rest and was spun for 12 years with no data assimilation. Forcing fields of the first year were based on monthly averages from Hellerman and Rosenstein (1983), the surface flux climatology of the Southampton Oceanographic Centre (Josey et al., 1998; Levitus, 2001). Years 2–12 of the spin-up were forced by momentum and heat fluxes from ERA-40 for the period 1994–2000 and by restoring salinity to Levitus (2001).

Analyses of the modelled trends during the spin-up run indicate that the globally-averaged near-surface circulation reached a state of quasi-equilibrium after about 3 years of integration. Interior transients below the thermocline and high-latitude temperature and salinity properties have much longer equilibrium time scales.

A complete description of the Bluelink Ocean Data Assimilation System (BODAS) is presented by Oke et al. (2005) and a comprehensive evaluation is contained in Oke et al. (2008a). The Appendix contains further details about BODAS. Briefly, BODAS assimilates all available satellite altimeters (ERS, GFO, Topex/Poseidon, Envisat and Jason), 57 coastal tide gauges around Australia, plus SST observations from Pathfinder and AMSR-E missions. *In situ* temperature and salinity observations are obtained from Argo floats, from the Tropical Atmosphere–Ocean (TAO) array, and from CTD and XBT (temperature only) surveys from a variety of different field surveys, including WOCE, Indian Ocean Thermal Archive (IOTA) and others.

2.1. Model skill

In order to gain confidence in the model results discussed in the subsequent section we briefly evaluate the impact of the reanalysis system and compare it with independent observations. Fig. 1 shows a sequence of monthly mean reanalysed sea level anomaly (SLA) maps from BRAN for each quarter of 2000. Overlayed on these maps are the surface drifter tracks for the one month period centered on the specified date in each panel. Data from the drifters were not assimilated into BRAN. This comparison therefore represents an independent qualitative assessment of how well BRAN reproduces the meso-scale variability around Australia. There is generally good correspondence between the drifter paths and the SLA fields, indicating that the surface eddy field around Australia is well represented by BRAN. By contrast, the equivalent SLA fields from the model-only run with no data assimilation (not shown) demonstrated no correspondence between the eddy-field and the drifter paths.

Fig. 2 shows a comparison between monthly mean SLA fields along the East Australian Coast from BRAN (top) and from objectively mapped fields produced by CLS (Ducet and LeTraon, 2000). These comparisons show good agreement, consistent with the findings of Oke et al. (2005), demonstrating that the observed SLA fields are generally well reproduced by the reanalysis.

To further elucidate the skill of the reanalysis system and particularly of the shelf circulation Table 1 shows a series of statistical comparisons between coastal SLA from BRAN and observations at coastal tide gauges around Australia. Specifically, Table 1 shows that the observed and reanalysed coastal SLA are well correlated (>0.8), with comparable standard deviation and relatively small root-mean square difference (RMSD). The RMSDs indicate that the difference between the observed and reanalysed coastal SLA is typically less than

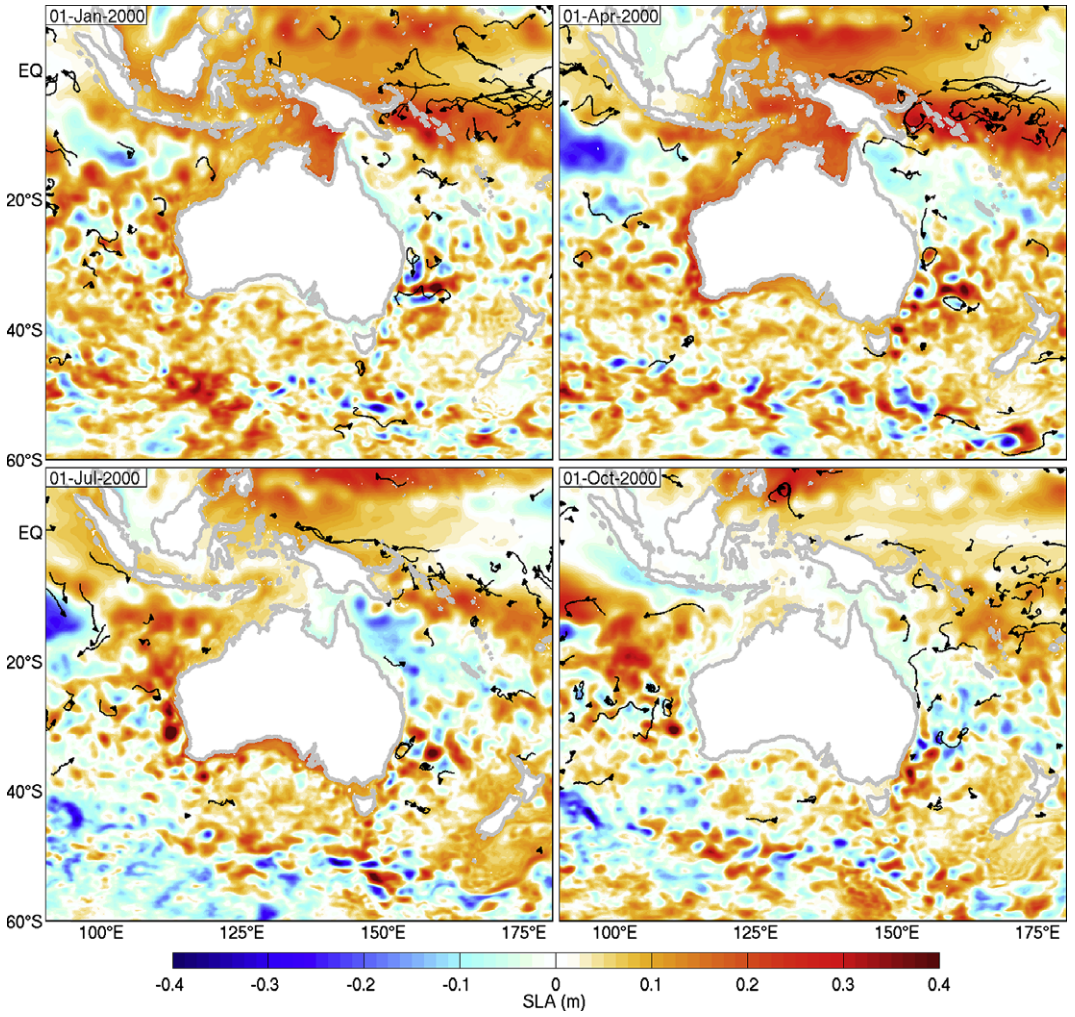

Fig. 1. A sequence of reanalysed sea-level anomalies (monthly means) from BRAN and surface drifter paths for the 1-month period centered at the specified date in 2000; negative anomalies (cyclonic) are red; positive anomalies (anti-cyclonic) are blue.

6 cm. We note that the assumed observation error for coastal SLA is typically between 3 and 4 cm (Oke et al., 2008a; see their Table 1). The comparisons in Table 1 demonstrate that BRAN quantitatively reproduces the shelf circulation that is represented here by coastal SLA.

3. The regional circulation

In this section we first provide an overview of the large-scale regional circulation on seasonal time scales. In the subsequent sections we discuss details of the circulation and transports in the areas of the Indonesian Throughflow (ITF), the Leeuwin Current (LC), the South Australian Current (SAC) and the East Australian Current (EAC) (Fig. 3a and b).

Schiller et al. (2006) provided a review about our current knowledge of the Indonesian Throughflow, which, until very recently, was largely based on single measurement campaigns to determine the near-surface geostrophic current structures. Ridgway and Condie (2004) documented the history of ocean dynamics off western and southern Australia, which goes back to the 19th century. Similarly, Ridgway and Dunn (2003) provided a comprehensive overview of our present understanding of the East Australian Current system.

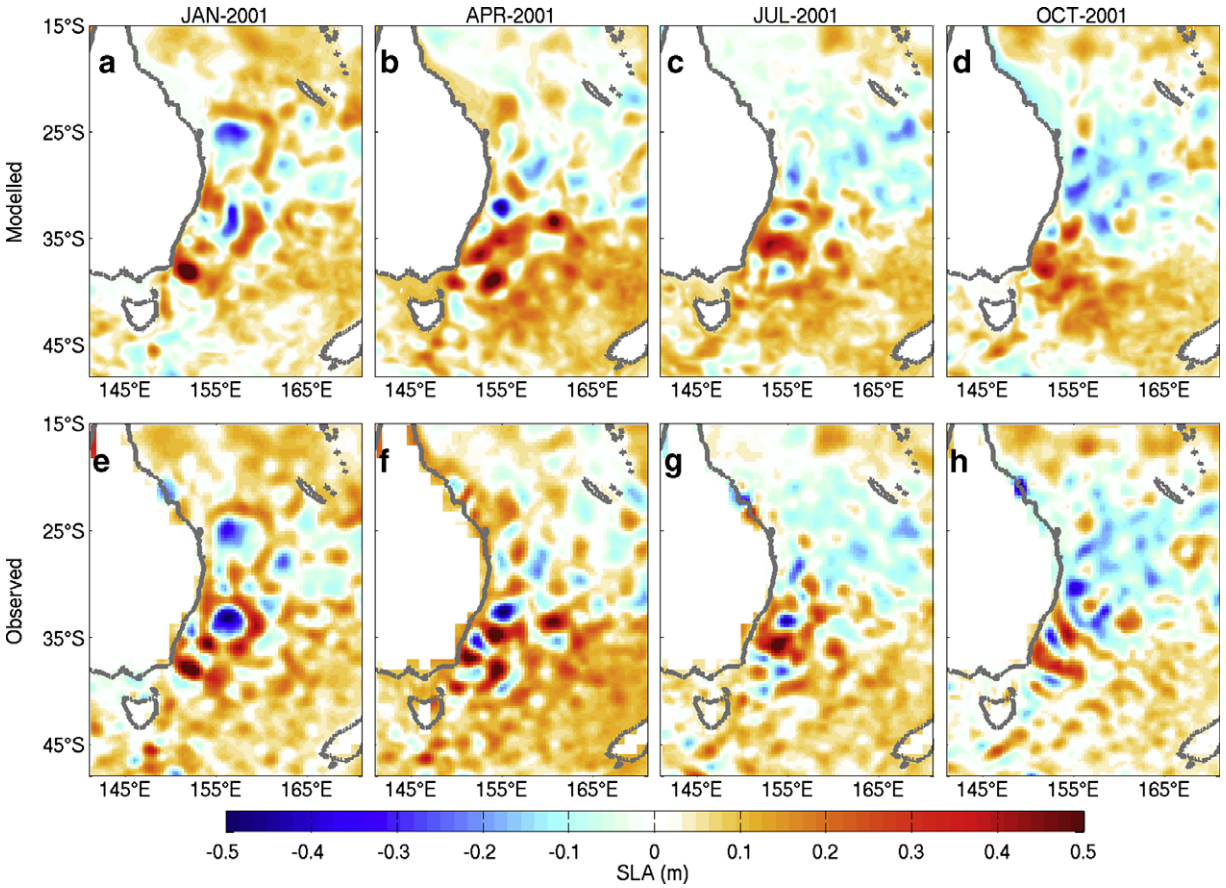

Fig. 2. Monthly mean reanalysed (a–d; from BRAN) and observed (e–h; from CLS, as described by Ducet and LeTraon (2000)) SLA every 3 months during 2001 off eastern Australia.

Table 1
Statistics of sea-level anomaly at coastal tide gauge stations around Australia

Coastline	*n*	BRAN std. dev.	Obs. std. dev.	CC	RMSD
East	31	9.1	9.8	0.81	5.8
South	7	9.7	11.0	0.92	4.0
West	19	11.0	13.0	0.94	4.6

See Oke et al. (2008a) for locations of tide gauges. Statistics are averaged for each coastline. The number of tide gauge stations (*n*) in coastal region is shown along with the average standard deviation from BRAN and observations (in cm), and the cross-correlation (CC) and root-mean squared difference (RMSD, in cm) between the BRAN SLA and the observed SLA. Note that one SLA observation from each tide gauge is assimilated into BRAN every 7 days, provided the observations are available.

Fig. 4 shows the near-surface circulation (0–100 m) for the months of January and July.[1] The dominant circulation features are the band-like structures of the western equatorial current system and the Antarctic Circumpolar Current (ACC). During January (Fig. 4a) the North Equatorial Current (NEC) and the cross-equatorial South Equatorial Current (SEC) enclose the North Equatorial Counter Current (NECC). At its western

[1] The analysis of seasonal features in this study is based on the period 1992–2001. This period coincides with the final years of the ERA-40 reanalysis which we regard as superior, in terms of quality-controlled surface forcing, to the operational ECMWF product we used as forcing fields for the subsequent years. We assess the differential impact of these two forcing fields on the ocean circulation in the discussion of transport time series.

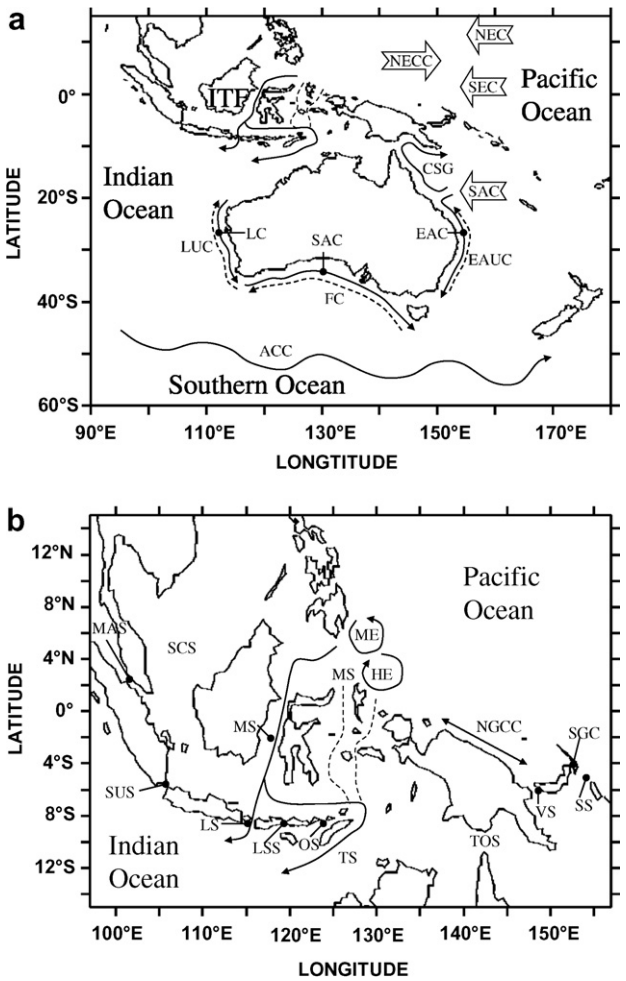

Fig. 3. Maps of the Asian–Australian Seas showing the major surface currents and straits as discussed in the text: Solid lines are surface currents: Indonesian Throughflow (ITF), Leeuwin Current (LC), South Australian Current (SAC), East Australian Current (EAC), Coral Sea Gyre (CSG), Antarctic Circumpolar Current (ACC), North Equatorial Current (NEC), North Equatorial Counter Current (NECC), South Equatorial Current (SEC), Mindanao Eddy (ME), Halmahera Eddy (HE), New Guinea Coastal Current (NGCC), Makassar Strait (MS), Lombok Strait (LS), Ombai Strait (OS), Timor Sea (TS), Vitiaz Strait (VS), St. George's Channel (SGC), Solomon Strait (SS), Molucca Sea (MS), Lesser Sunda Straits (LSS), Sunda Strait (SUS), Malacca Strait (MAS), Torres Strait (TS). Dashed lines are (largely) subsurface currents: Leeuwin Undercurrent (LUC), Flinders Current (FC), East Australian Undercurrent (EAUC).

boundary the Mindanao Eddy dominates the near-surface circulation at the entry of the ITF. Strong surface currents driven by the North-East Monsoon are evident in the South China Sea. Most of this eastward flow reaches the Banda Sea and leaves the ITF through the Lesser Sunda Straits en route to the Indian Ocean. During July (Fig. 4b) the near-surface circulation at the equator is less structured. The New Guinea Coastal Current feeds the Halmahera Eddy which is the source of the NECC. In the ITF area jet-like structures in Makassar and Lombok Straits and in the Savu and Timor Sea denote the main paths of the ITF.

Figs. 5 and 6 show observed and simulated surface eddy kinetic energies (EKEs) for January 1996 west and east of about 145°E. Altimetry (Figs. 5a and 6a) represents the thermocline circulation below the surface Ekman-layer. We used velocity fields from the model at a depth of 45 m to calculate kinetic energies and to make the signals comparable with the observations (kinetic energy $(\mathrm{KE}) = 0.5(u^2 + v^2)^{1/2}$). Eddy kinetic energy was calculated by subtracting the long-term mean from the total velocity field. Consequently, the eddy kinetic energy as defined in this study contains seasonal and shorter term fluctuations.

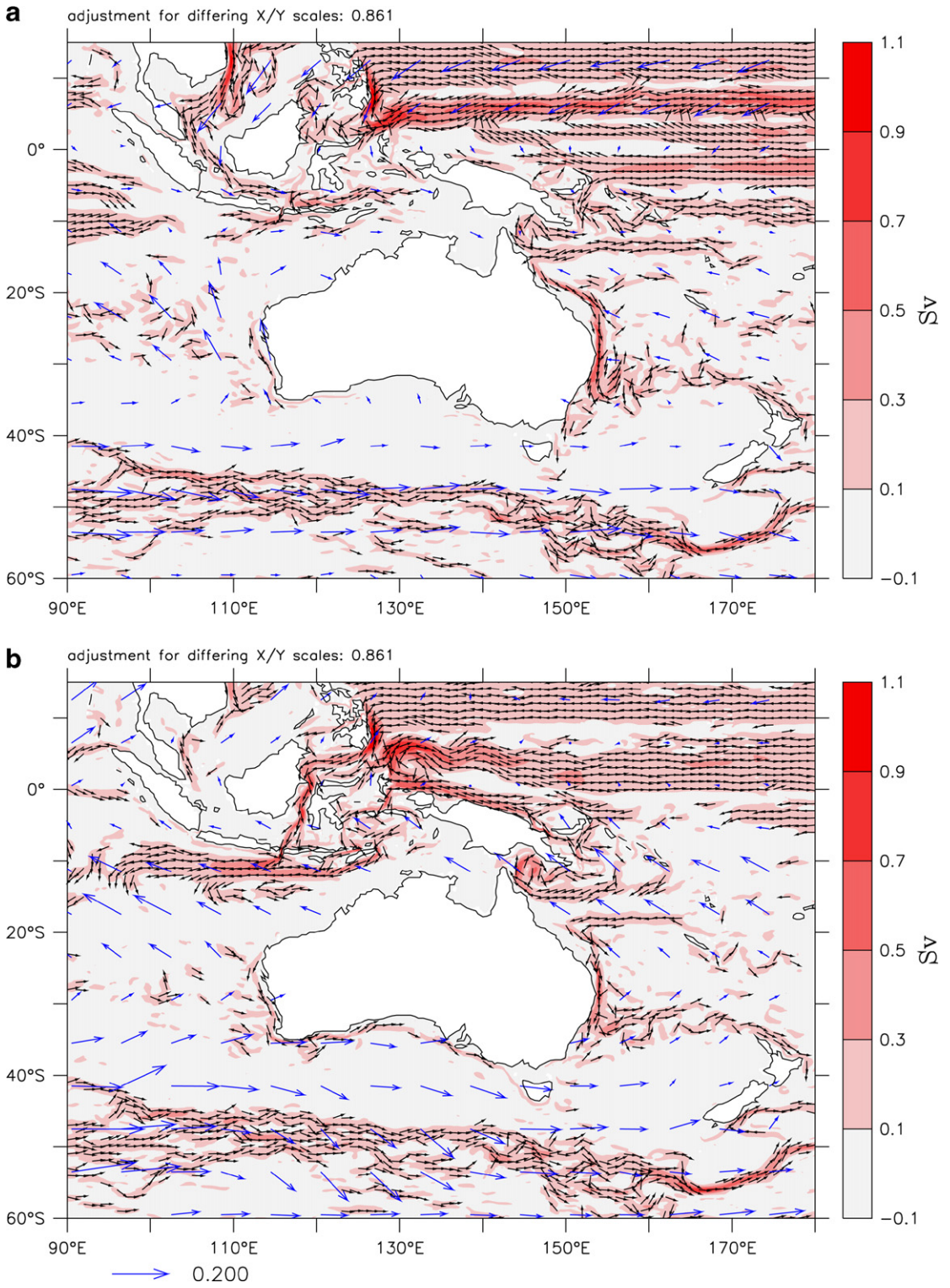

Fig. 4. Volume transports (black arrows for direction, red colour for amplitude) in each 1° box integrated over top 100 m from BRAN for (a) January and (b) July (1 Sv = 10^6 m^3/s). For clarity, transports in excess of 1.1 Sv have been clipped. Unit vectors show direction of transport >0.1 Sv. Superimposed in blue color are climatological surface wind stresses (Josey et al., 1998). Wind stress vector scale is shown at bottom (N/m^2).

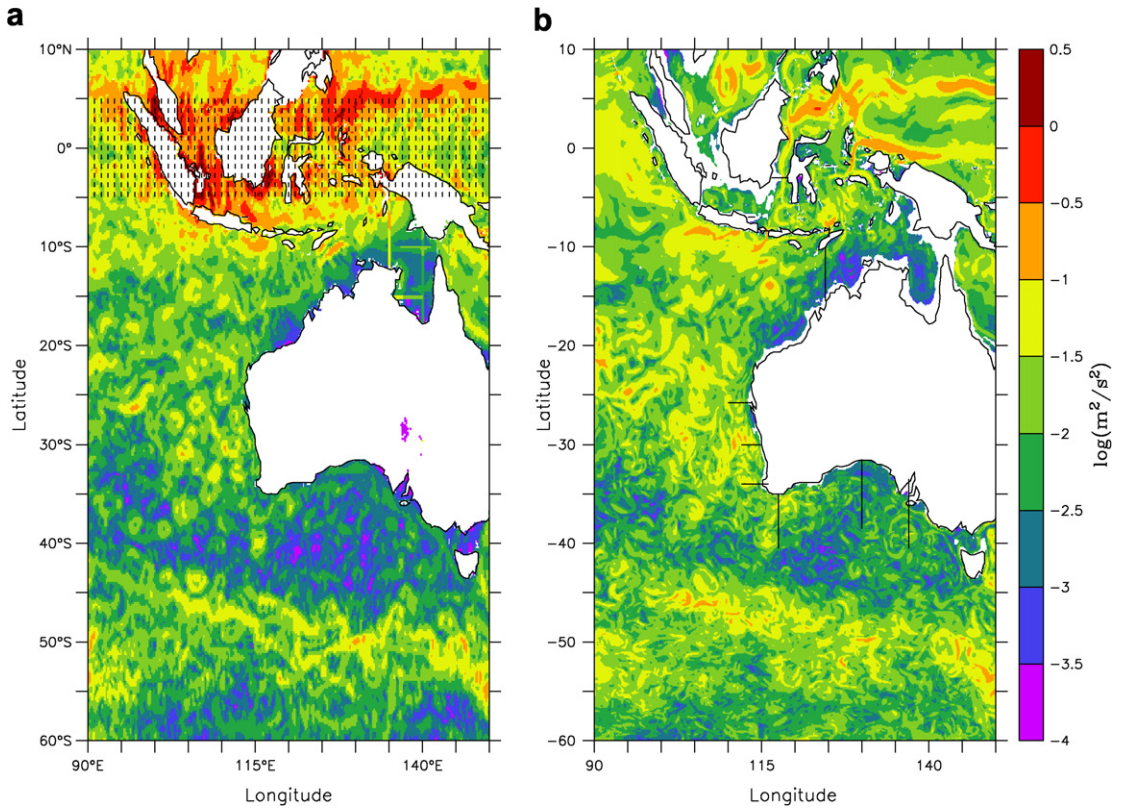

Fig. 5. Logarithm of surface eddy kinetic energy in Indonesian Throughflow and southeast Indian Ocean for January 1996: (a) merged satellite altimetry (ERS, Topex/Poseidon); (b) reanalysis. Shaded area in (a) denotes equatorial region where eddy kinetic energy derived from observations of sea-level anomalies is less reliable due to break-down of geostrophic momentum balance. Black lines in (b) indicate vertical sections discussed in subsequent text. Units are in m^2/s^2.

West of 145°E observed maxima of EKE are found in the tropical region (Fig. 5a) with values exceeding 1 m^2/s^2 (Ducet and LeTraon, 2000). However, these estimates are less reliable than those away from the equator due to approximations which need to be applied to the geostrophic momentum balance in tropics, resulting in less accurate estimates of EKE. A second, but less pronounced broad band of maximum EKE exists along the axis of the ACC. The reanalysis (Fig. 5b) reproduces these features but underestimates the spatial extent of high amplitudes of EKE in the tropics. Along the LC the EKE of the reanalysis is slightly stronger than observed, as it is in the Great Australian Bight (GAB). The grid structure to the north of Australia is due to missing data (satellite failure) in January 1996.

In the eastern part of the eddy-resolving domain the altimetric EKE shows maxima along the north- and south-equatorial current systems, the EAC and the ACC (Fig. 6a). Amplitudes of EKE from the reanalysis (Fig. 6b) along the EAC and ACC resemble those from observations whereas the reanalysis again underestimates the extent of large EKE along the equatorial belt. EKEs in the Tasman Sea and around New Zealand are slightly smaller in the reanalysis than in the observations. Although the exact reason for this discrepancy is unknown we verified that the local wind forcing at these latitudes applied to the model is too weak and is the most likely culprit for this discrepancy. Another possible explanation is the lack of sufficiently strong inflow of EKE from outside the eddy-resolving model domain. Both notions are supported by a model simulation without data assimilation where these areas (plus the SEC) also show weaker than observed EKEs (not shown).

The ratio of eddy-to-total kinetic energy of the reanalysis reveals some interesting features (Fig. 7). Firstly, most of the region is dominated by eddy kinetic energy. Nevertheless, both the equatorial current system (with the exception of the transition zones between SEC, NECC and NEC) and the ACC have about equal contribution from eddy and mean kinetic energy during the whole year. Topographic steering south and east of New

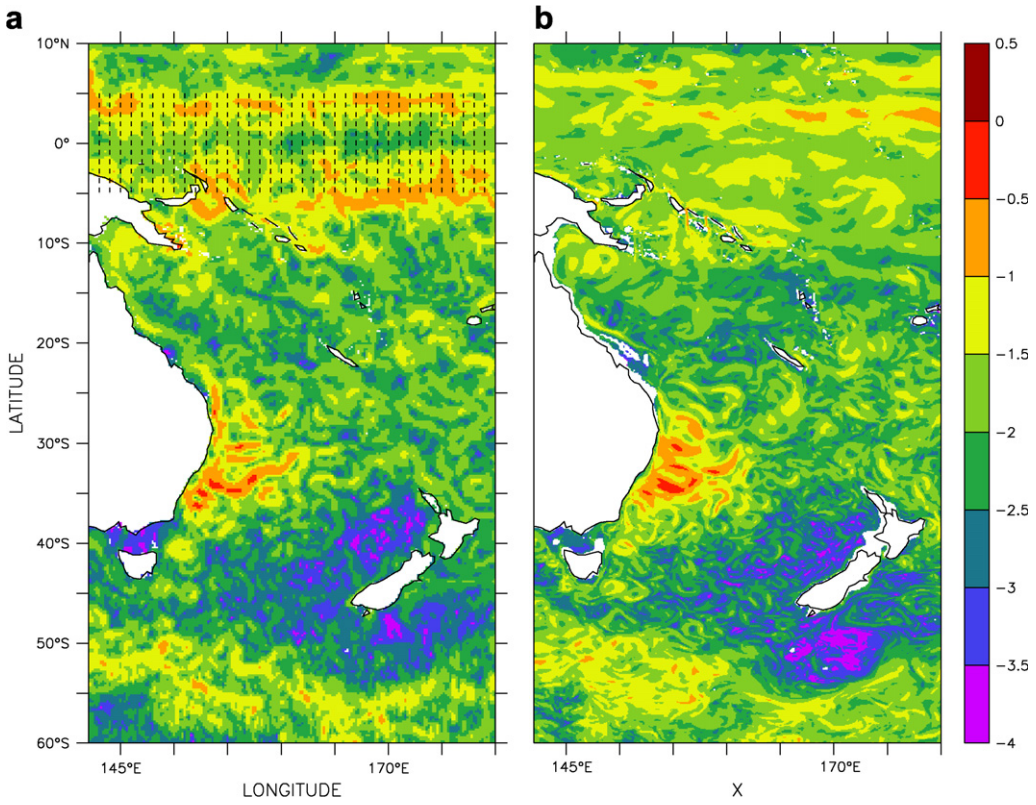

Fig. 6. As in Fig. 5 but for Southwest Pacific region.

Zealand leads to narrow bands of strong mean kinetic energy (Morrow et al., 1994). Similar features can be found in July (Fig. 7b) in the Arafura Sea and along the Great Barrier Reef and Coral Sea Gyre (Burrage, 1993). In July the ITF appears as a current dominated by mean kinetic energy rather than by eddies as in January (Fig. 7a). Furthermore, a narrow band of shelf edge currents exists around Australia, which starts off Northwest Cape, follows the LC and SAC, passes through Bass Strait and around the southern tip of Tasmania, and ultimately ends up in the Tasman Sea (Ridgway and Condie, 2004).

3.1. The Indonesian Throughflow system

The Indonesian Throughflow (ITF) is the only low-latitude connection between two major oceans and therefore represents a choke-point in the global distribution of heat and freshwater in the climate system. More specifically, it is an important source of heat and salt for the Indian Ocean and therefore has important impacts on both regional and global climate (CLIVAR-GOOS Indian Ocean Panel and collaborators, 2005). Direct current measurements in the Indonesian Archipelago are available for only a few locations and are often of short duration. Despite numerous attempts to measure the ITF transport of water-mass, heat and salt over the last 20 plus years, the largely uncoordinated efforts have not produced a coherent picture of the circulation (Godfrey et al., 1995), owing to the difficulty of making the measurements in a complex topography and highly variable current system (CLIVAR-GOOS Indian Ocean Panel and collaborators, 2005). A multinational group of scientists and agencies started a project called INSTANT in 2003 with the goal to accurately describe the ITF and its transport of mass, heat and fresh water by direct measurement for a period of three years (Sprintall et al., 2004). This project will deliver an unprecedented data set for model validation but has not yet produced data that could be exploited in the reanalysis described in this paper.

Analysis of observations indicates that the ITF exists because the southeast and northeast trade winds over the Pacific pile up the warm equatorial waters against Indonesia, creating a pressure gradient between the

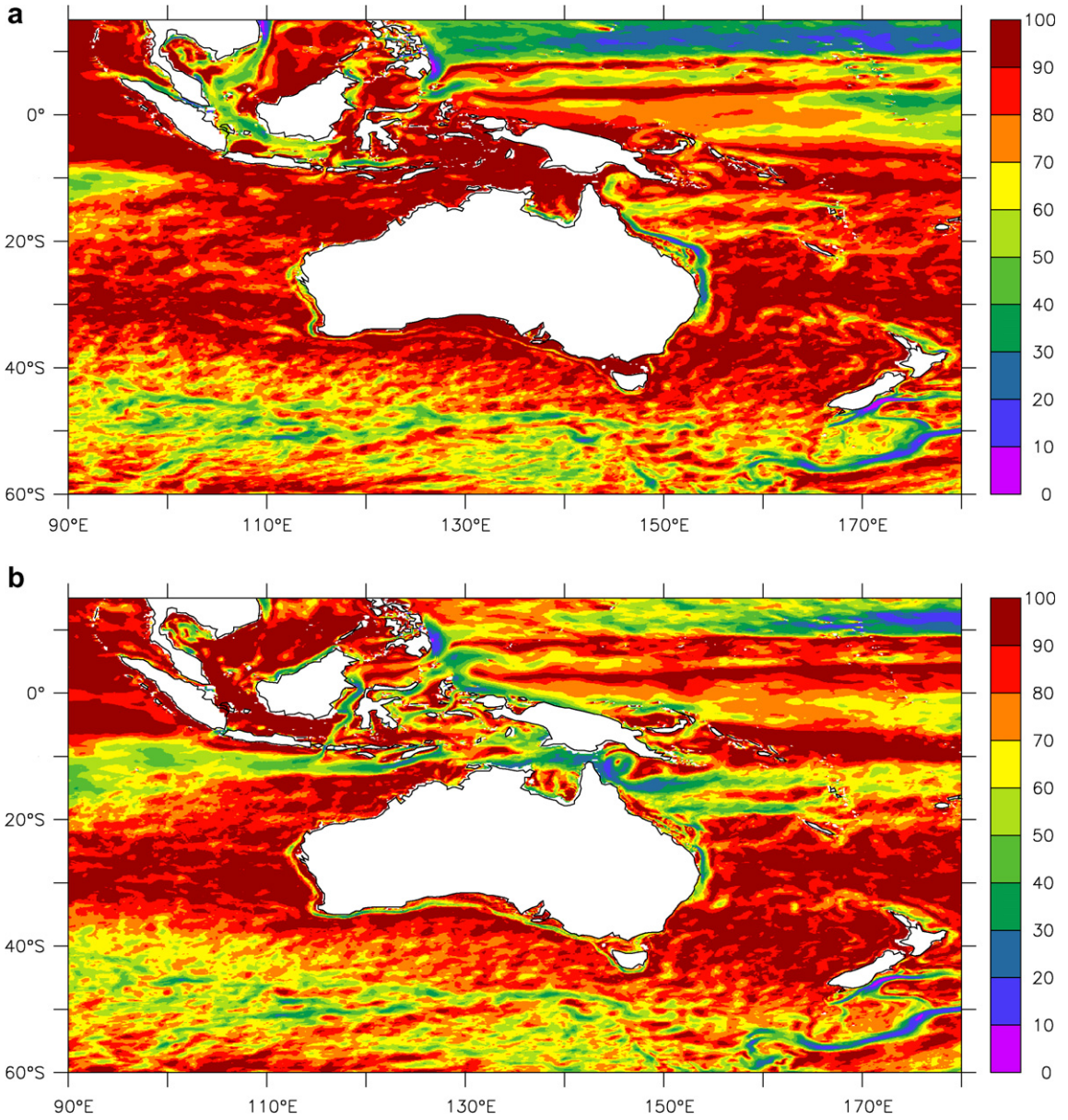

Fig. 7. Ratio of eddy kinetic energy to total kinetic energy from reanalysis: (a) January; (b) July. Monthly values were calculated as long-term means over the whole period of the reanalysis. Units are in %.

western Pacific boundary and the eastern Indian Ocean (CLIVAR-GOOS Indian Ocean Panel and collaborators, 2005). The gradient is maintained between the two sides of the Indonesian archipelago and this drives a flow through numerous passages between the islands that connect the Pacific and Indian Oceans and the internal Indonesian seas. As the ITF leaves the Indonesian archipelago, it merges with the South Indian Ocean current system. The ITF is known to be highly variable on intraseasonal to decadal time-scales, making it a particularly difficult flow to observe. Furthermore, the many straits of the ITF are narrow (e.g. Lombok Strait is less than 50 km wide) and can only be adequately resolved by high-resolution OGCMs.

The ITF is composed mostly of North Pacific water flowing through Makassar Strait (Gordon and Fine, 1996). A small part enters the Indian Ocean through Lombok Strait while the bulk of the ITF turns eastwards through the Flores and Banda Seas and enters the Indian Ocean around Timor (Fig. 8a and b). The Lombok

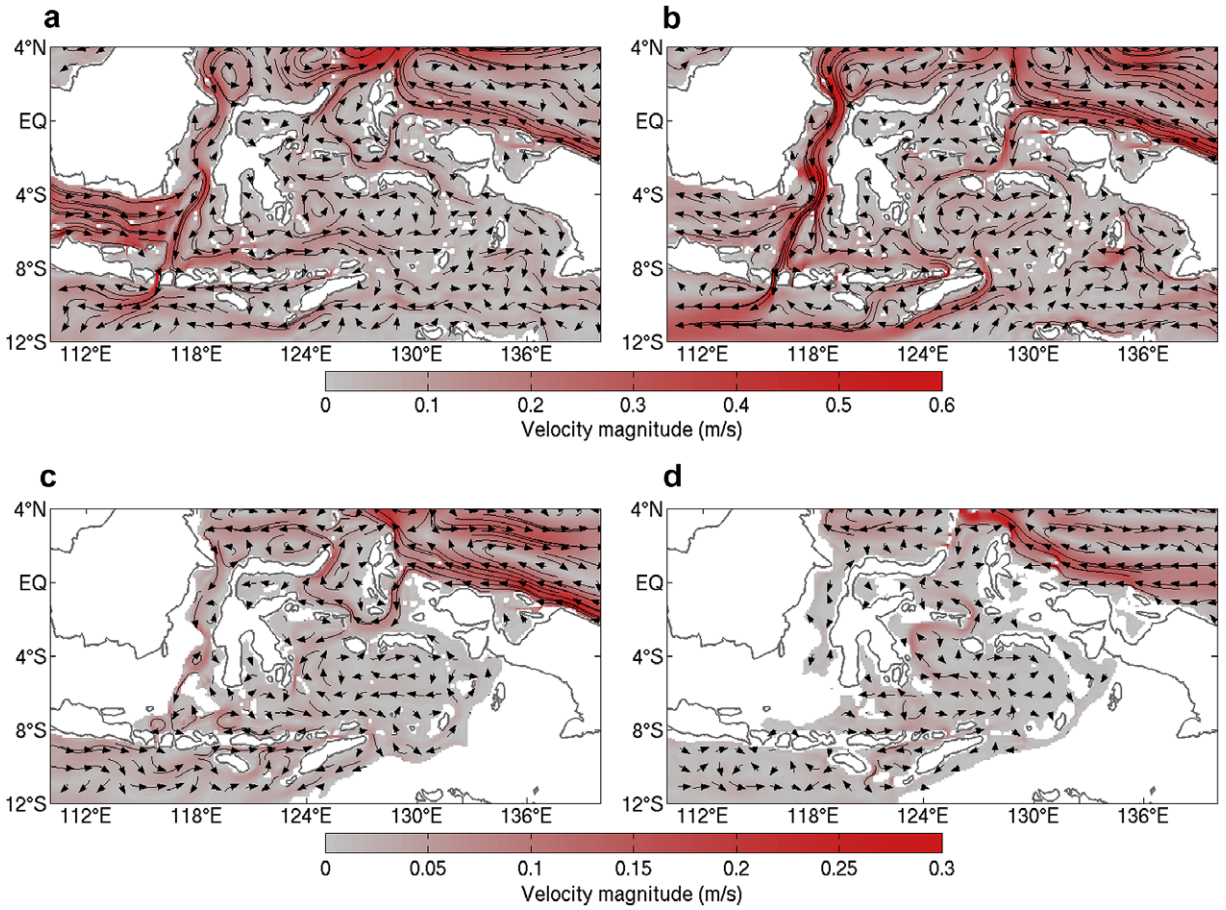

Fig. 8. Seasonal circulation in the Indonesian Throughflow area showing the depth-averaged circulation at 0–250 m for January (a) and July (b); and annual mean circulation at the thermocline depth (250–500 m) (c); and annual mean circulation at intermediate depth (800–1200 m) (d). Colours show the magnitude of the currents (m/s). Every 10th vector is shown. Vector lengths correspond to 20 (a, b) and 40 (c, d) day Lagrangian trajectories.

Strait is 350 m deep and thus passes only the upper layer water-masses. A small amount of deeper water of South Pacific origin flows through the eastern passages, via the Molucca and Halmahera Seas. From the Banda Sea there are two deep passages to the Indian Ocean, the Ombai Strait and the Timor Passage with sills at about 800 m and 1200–1300 m respectively (Fig. 8c and d). Other connections between the Indonesian Archipelago with negligible transports are the Strait of Malacca, Sunda Strait and flow through the passages of the Lesser Sunda Island chain.

The meridional velocity profile in Makassar Strait (Fig. 9a and b) has strong seasonality in vertical shear above 150 m, as observed by Gordon et al. (2003). Qu et al. (2005) recently attributed the northward near-surface flow during boreal winter to wind-driven advection of water-masses from the South China Sea ($|v_{\max}| > 0.2$ m/s). During the Northeast Monsoon over the South China Sea (Fig. 4a) these water-masses create a northward pressure gradient in Makassar Strait that inhibits warm surface water from the Pacific flowing southward into the Indian Ocean. In July the transports through Makassar Strait are predominantly southward ($|v_{\max}| > 0.8$ m/s), but a subsurface maximum is found in both seasons.

Seasonal transports through Lombok Strait (Fig. 9c and d) are almost completely southward over the whole depth range and have maxima at about 150 m in January ($|v_{\max}| > 0.9$ m/s) and near the surface in July ($|v_{\max}| > 1.6$ m/s). For visual purposes the narrowest but not shallowest section across the simulated Lombok Strait is shown. Both Lombok Strait and Makassar Strait transports show a western intensification. Ombai Strait depicts a seasonal reversal of the velocity at the surface (Fig. 8e and f) with the surface circulation likely

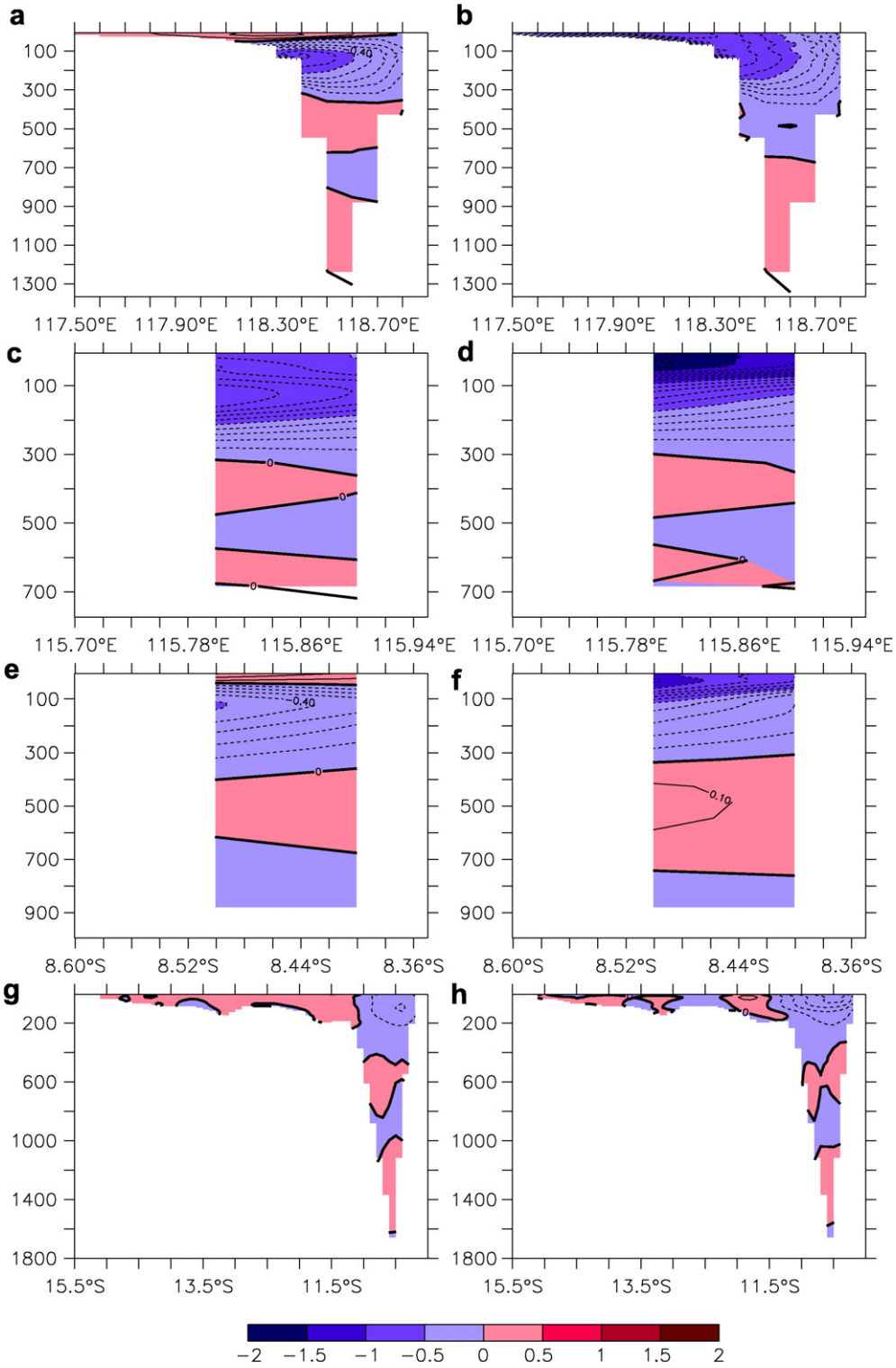

Fig. 9. Seasonal circulation of Indonesian Throughflow: vertical sections across Makassar Strait (3°S) (a, b), Lombok Strait (8.4°S) (c, d), Ombai Strait (125.1°E) (e, f), and Timor Strait (124.5°E) (g, h) for January (left column) and July (right column). Red (blue) color in (a–d) shows northward (southward) currents; red (blue) color in (e–h) shows eastward (westward) currents. Contour interval of isolines is 0.1 m/s. See Fig. 5 for geographical location of sections.

driven by local wind patterns (Fig. 4). During austral summer a wind-driven eastward surface current flows counter to a deeper westward thermocline circulation. In austral winter a strong westward current at the surface down to the thermocline ($|v_{max}| > 1.2$ m/s) sits on top of a deep eastward current. Transports through the Timor Passage show a similar intensification of westward transports in the thermocline during austral winter (Fig. 9g and h).

The mean transport of the ITF is now believed to be about 10 Sv and it has a marked seasonal cycle with a maximum in August–September (CLIVAR-GOOS Indian Ocean Panel and collaborators, 2005). These conclusions are based on various data collected before INSTANT, including year-long time-series in Makassar Strait, flow through the passages of the Lesser Sunda Island chain, repeated XBT sections between Java and Australia, direct deep-current measurements and WOCE sections between Australia and Indonesia (e.g., Meyers et al., 1995; Molcard et al., 1996). Direct measurements during 1997 indicated that the ITF varies in strength with the phase of ENSO (Susanto and Gordon, 2005). Based on a 15-month-long mooring time series these authors reported ITF transports as small as 4.6 Sv (and larger than 10 Sv) during El Niño (La Niña). Application of the island rule (Godfrey, 1989) to Australia–New Guinea and using the ERA-40 winds yields a mean transport estimate of 14.6 Sv (Qu et al., 2005).

In Fig. 10 total transports integrated across the main pathways of the ITF are shown. Table 2 contains further details on the transports through the ITF as derived from the ocean reanalysis. Transports through Makassar Strait show a distinct seasonal signal with a minimum in December during the Northwest Monsoon (−4.1 Sv) and a maximum in September during the Southeast Monsoon (−11.9 Sv) (Fig. 10a). The mean and standard deviation of simulated Makassar Strait transport are -8.4 ± 3.8 Sv. The time series of Makassar Strait transport is dominated by annual and interannual variability. A distinct feature is the interannual variability with, e.g., minimum transport at the height of the 1997/1998 El Niño event.

As seen in Figs. 4 and 8 a notable fraction of the ITF (and of Makassar Strait transport) enters the Indian Ocean through Lombok Strait. On average -1.5 ± 1.2 Sv are advected through this narrow and shallow strait (Fig. 10b). The weak semi-annual cycle of transport through Lombok Strait reveals minima in May and November and maxima in March and July. Interannual variability in the daily time series of Lombok Strait transports is weak. However, Lombok Strait also represents a wave guide for processes on intraseasonal-to-interannual time scales originating in the Pacific as well as Indian Oceans (Sprintall et al., 1999; Wijffels and Meyers, 2004). Consequently, the power spectrum of the transport time series shows various maxima around periods of 3, 6 and 12 months and on interannual time scales (not shown).

Similar interannual features are found in the transport through Ombai Strait (Fig. 10c; annual mean $= -1.5 \pm 1.2$ Sv) but the seasonal signal is weak. Transports through the Timor Sea (Fig. 10d) show a distinct annual signal (mean $= -6.0 \pm 3.3$ Sv) with a minimum in January (−2.8 Sv) and a maximum in April (−8.8 Sv). The distinct seasonal signal is also visible in the daily time series. The volume transport through Timor Sea contains spectral peaks at semi-annual, annual and interannual periods (not shown).

The total transport through all topographic gaps between the Indonesian archipelago and the Indian Ocean is -9.7 ± 4.4 Sv (January: −6.6 Sv, April: −12.3 Sv). This is weaker than the mean transport estimate of (−)14.6 Sv based on the "island rule" (Godfrey, 1989) using the ERA-40 winds (Qu et al., 2005). However, on intraseasonal and short time scales the simulated ITF is associated with significant fluctuations which range from +5.0 Sv (out of Indian Ocean) to −25.7 Sv (into Indian Ocean).

These fluctuations are also associated with a temporal bias in the surface wind stress fields which starts in 2002 and is associated with changes in wind stress forcing used by the model. An examination of the ERA-40 winds (1992–2001) and the operational winds (2002–2006) reveals some increases on the large-scale 4-year mean wind stress fields ($\Delta\overline{|\tau|} \leqslant 0.02$ N/m^2) which caused stronger Ekman transports in the latter period, resulting in a notable change in the total transport through, e.g., the ITF: from 1992 to 2001 the mean transport and associated variability of the ITF is -8.4 ± 4.1 Sv whereas for 2002–2006 the mean transport increases to -12.5 ± 3.9 Sv. A detailed comparison of the forcing fields and their impacts on the ocean circulation on interannual time scales is beyond the scope of this study.

Nevertheless, our 14-year-long mean transports are in good agreement with sparse observation-based estimates of ITF transports. For example, Susanto and Gordon (2005) quote a total depth-integrated transport of (−)8.1 ± 1.5 Sv from a 20-month-long mooring in Makassar Strait in the late 1990s, which compares to

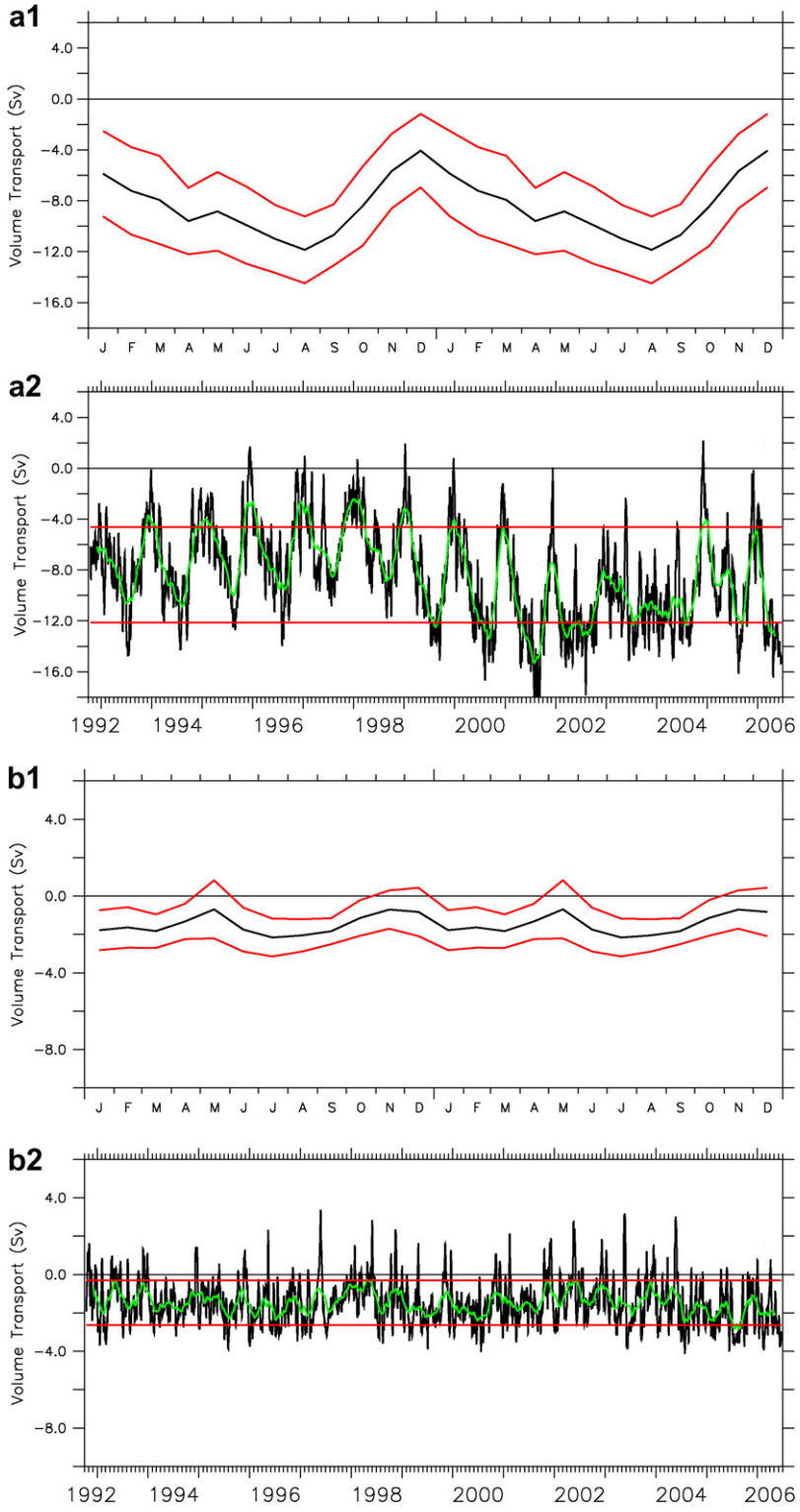

Fig. 10. Total transports of major paths to Indian Ocean for period October 1992 to June 2006: (a) Makassar Strait; (b) Lombok Strait; (c) Ombai Strait; (d) Timor Sea. (a1, b1, c1, d1): seasonal cycle, (a2, b2, c2, d2): daily-averaged time series. Red lines indicate plus/minus one standard deviation. Green lines denote 3-months running means. Units are in 10^6 m^3/s.

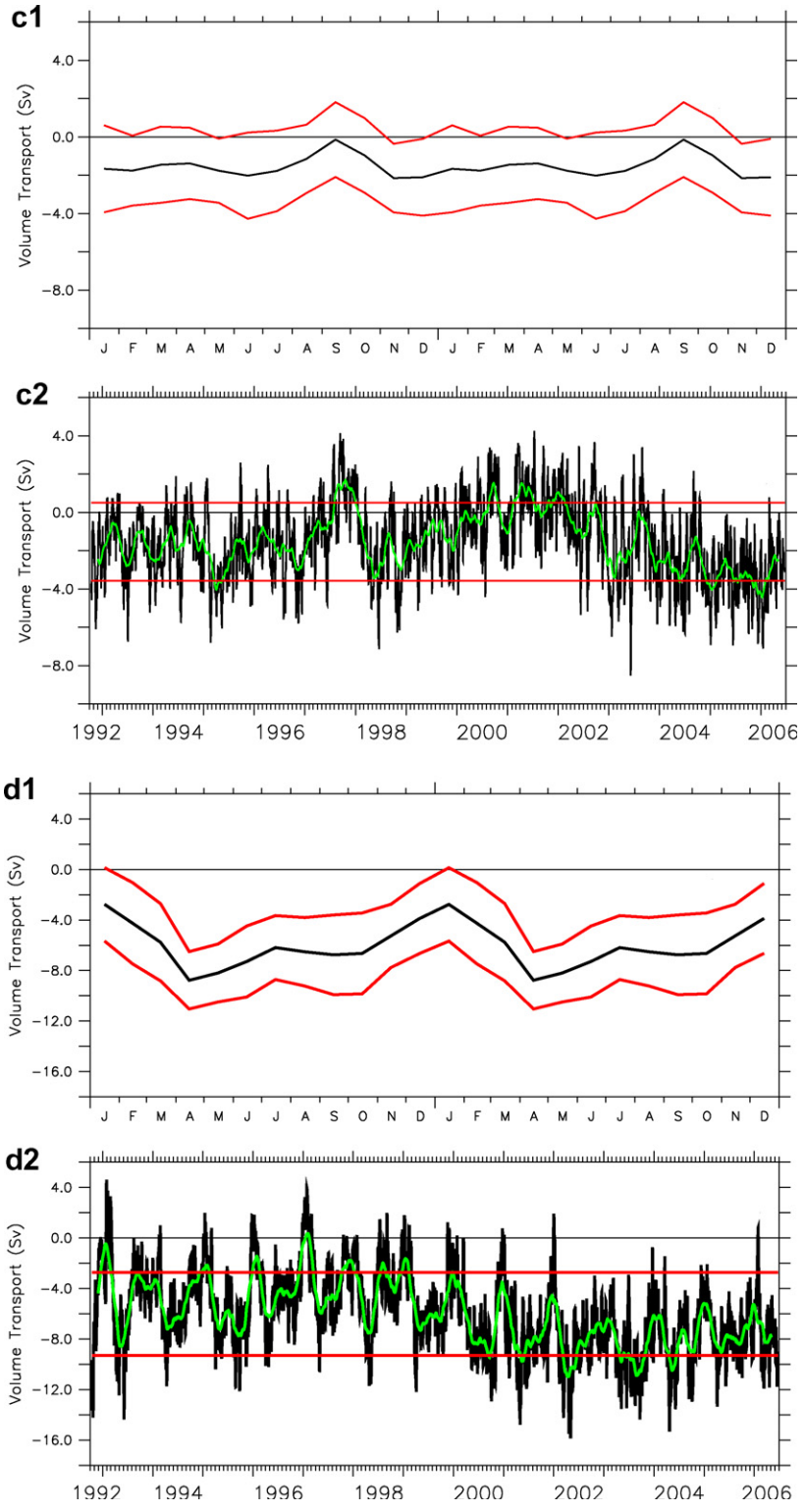

Fig. 10 (*continued*)

Table 2
Depth-integrated transports in Indonesian Throughflow

	Range (Sv;1 Sv = 10^6 m^3/s)	Mean and std. dev. (Sv)
Makassar Strait[a]	+2.2 to −18.9	-8.4 ± 3.8
South China Sea[a]	+4.3 to −8.0	-1.7 ± 2.1
Halmahera Sea[a]	+8.6 to −15.2	-5.8 ± 3.5
Molucca Sea[a]	+22.4 to −19.4	$+4.3 \pm 5.5$
Lombok Strait[a]	+3.6 to −4.2	-1.5 ± 1.2
Ombai Strait[b]	+4.4 to −8.9	-1.5 ± 2.1
Timor Sea[b]	+4.6 to −16.5	-6.0 ± 3.3
Sunda Strait[b]	+0.8 to −1.0	-0.4 ± 0.3
Lesser Sunda Straits[a]	+1.2 to −1.2	-0.3 ± 0.5
Malacca Strait[a]	+0.8 to −0.4	$+0.2 \pm 0.2$
ITF total[c]	+5.0 to −25.7	-9.7 ± 4.4

[a] Positive (negative) values indicate northward (southward) transports.
[b] Positive (negative) values indicate eastward (westward) transports.
[c] Negative values indicate transports from Pacific to Indian Ocean.

-8.4 ± 3.8 Sv from our reanalysis. The model results will be subject to further validation once the full time series of the INSTANT program mentioned previously becomes available.

3.2. The Australian Current systems

3.2.1. The Leeuwin Current system

The Leeuwin Current (LC) is highly seasonal, peaking in austral autumn and winter, but is weaker in austral summer when it flows against prevailing southerly winds (Fig. 4). The anomalous Leeuwin Current has a strong influence on the evolution of the regional marine ecosystems (Griffin et al., 2000). Through its suppression of large-scale upwelling by opposing transport of warm tropical waters the Leeuwin Current makes the inshore environment of the western coast to be much warmer than it would be otherwise. Near Perth (32°S) the average sea surface temperature is about 5 °C warmer than the average temperature at the same latitude off the other two western coasts in the southern hemisphere (Feng et al., 2003).

One source of the LC is of Pacific origin (Figs. 8 and 11a,b) via the ITF. This Pacific Ocean water is warmer and lower in salinity than the subtropical Indian Ocean. The associated sea level in the north-east Indian Ocean is about 55 cm higher than the sea level of the cool and dense Southern Ocean near Cape Leeuwin (35°S). The resulting steric height (pressure) gradient is the main driving force of the southward flowing LC (Tomczak and Godfrey, 1994). This creates an onshore geostrophic flow which also draws water from the Indian Ocean towards the coast. As this water reaches the shelf-break it turns towards the south with the LC (Tomczak and Godfrey, 1994) (Fig. 11a and b). The strength of the LC is augmented by interactions with a series of quasi-permanent eddies/jets further offshore which have detached from the boundary flow of the LC. Feng et al. (2005) showed that the ITF not only provides the driving mechanism for the unique poleward flowing LC, but also drives the strongest eddy kinetic energy among all eastern boundary currents. The predominantly warm core eddies transfer the bulk of heat from the LC along the coastal region off Western Australia into the southeast Indian Ocean Subtropical Gyre (Fang and Morrow, 2003; Domingues et al., 2006).

Due to the impact of eddies on the mean circulation it can be difficult to identify distinct longer-term signals in boundary currents. We therefore focus our discussion of transports on the residual circulation associated with boundary currents, i.e. without pre-selecting a particular direction and unless noted otherwise. Around North-West Cape (near 22°S) the LC first takes on the shape of a narrow, but well-defined southward flow of tropical water (Fig. 12a and b). At 25.8°S the LC is less than 300 m deep, up to 200 km broad and with seasonal velocities of up to 0.3 m/s.

The core of the LC is located just off the shelf-break (Figs. 11a,b and 12) and its strength varies between seasons. During August–September, strong and consistent winds from the south (Fig. 4a) begin to dominate the western coast. These last until February–March and reduce the strength of the LC (Figs. 11a, 12c and 13).

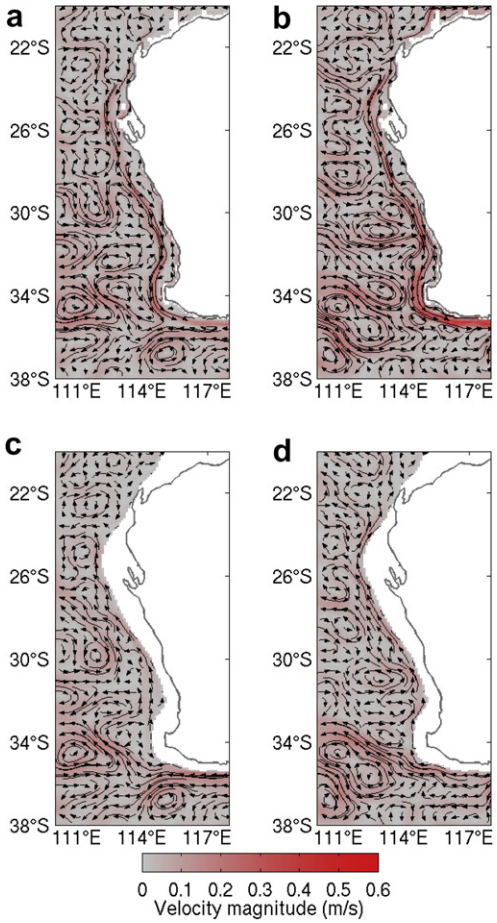

Fig. 11. Seasonal circulation off western Australia showing the depth-averaged circulation at 0–250 m (a, b), and at 250–500 m (c, d) for January (left column) and July (right column). Colours show the magnitude of currents (m/s). Every 5th vector is shown. Vector lengths correspond to 14 day Lagrangian trajectories.

After the southerlies subside at 34°S the LC rapidly strengthens and remains strong until July (maximum southward velocity at surface above 0.4 m/s; Figs. 11b, 12f and 13b).

The simulated seasonal cycle at 34°S (Fig. 13b) is in good agreement with a recent analysis of the LC at 32° (Feng et al., 2003). The southward transport is about 3–5 Sv during austral summer months and peaks at 4.8 Sv in June with a mean of -3.1 ± 2.6 Sv (Table 3). The mean transport of the LC is strongly influenced by large eddy activity (Fig. 7), and the seasonal cycle is more complex, particularly further north (Fig. 13a).

Inshore of the LC relatively shallow waters are strongly influenced by local winds and therefore often flow northward with the prevalent southerlies – in the opposite direction to the LC (Fig. 12c and e). At 30°S the simulated shelf current (Capes Current) flows northward between August and April at a maximum velocity of about 0.2 m/s. Underneath the LC exists the slow and cool northward-flowing Leeuwin Under Current (LUC) (Thompson, 1984). The simulated LUC exists throughout the year with a variable core depth between 200 and 600 m (Fig. 11c and d) and a velocity maximum of about 0.1 m/s between October and January as observed by Domingues (2006).

The Leeuwin flow is closely linked with the El Niño–Southern Oscillation (ENSO) cycle, being weaker during El Niño years when the ITF is reduced (Feng et al., 2003). For instance, in the reanalysis top-to-bottom transports at 34°S (Fig. 13b) correlate at 0.7 with a lag of about 6 months with NINO34 and SOI indices. During an El Niño episode the reduced depth of the thermocline in the western Pacific decreases the pressure

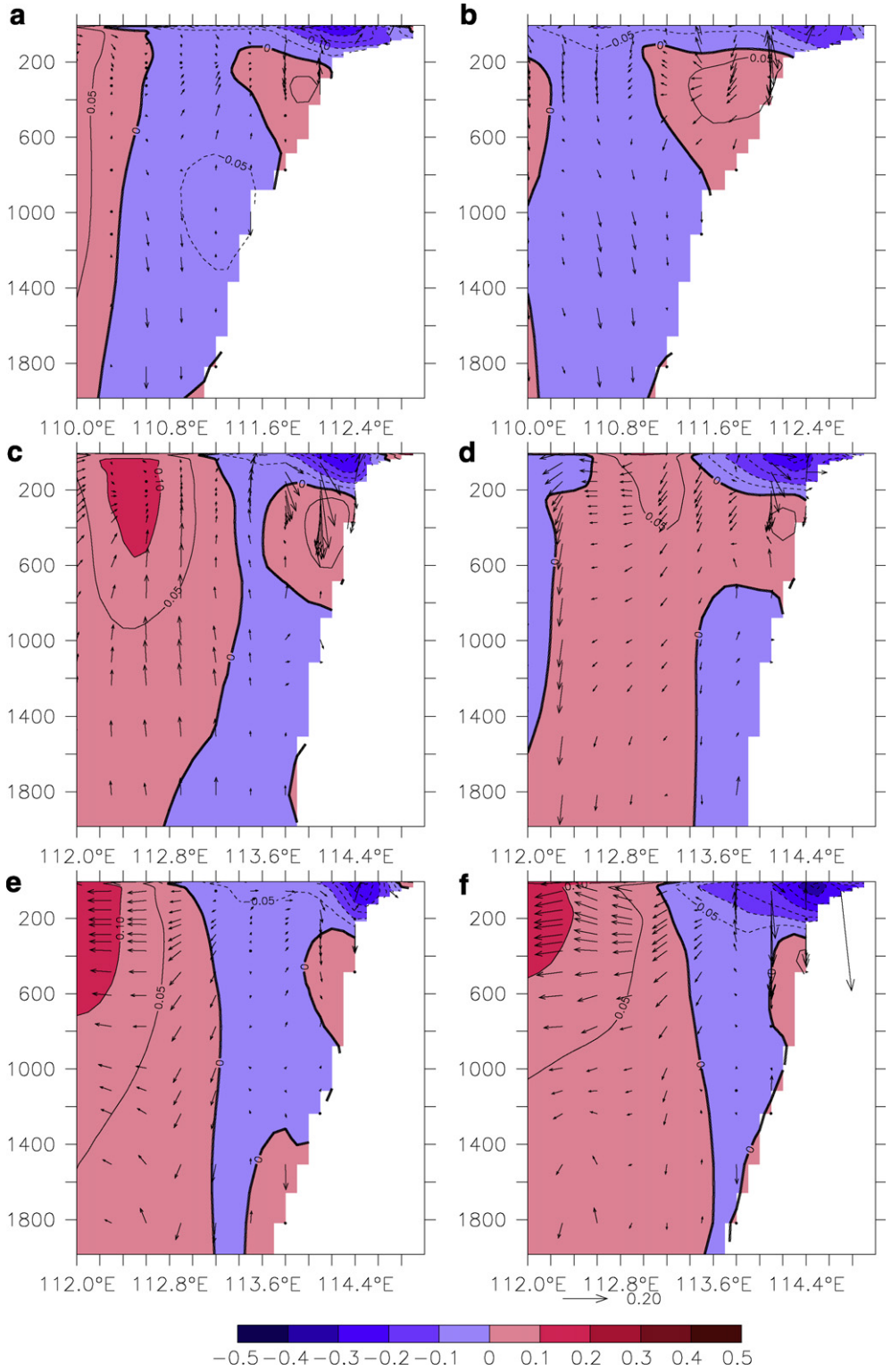

Fig. 12. Seasonal circulation off western Australia: vertical sections (0–2000 m) at 25.8°S (a, b), 30°S (c, d), and 34°S (e, f) for January (left column) and July (right column). Red (blue) color shows northward (southward) currents. Contour interval of isolines is 0.05 m/s. Circulation in (u, w) plane is superimposed as vectors (w component re-scaled by a factor of 5000). Reference vector is shown underneath (f). See Fig. 5 for geographical location of sections.

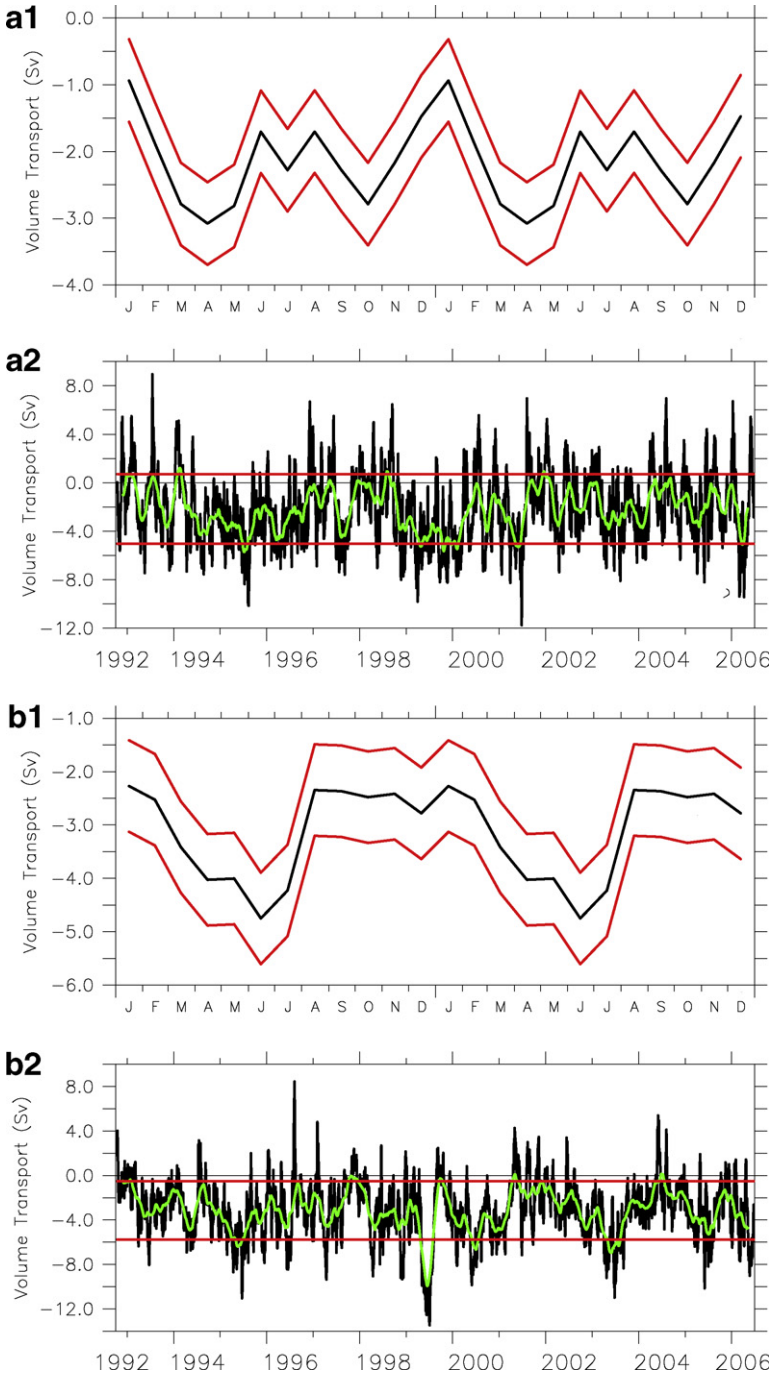

Fig. 13. Total transports of Leeuwin Current System (0–300 m, 113.5°E to 115.0°E) for period October 1992 to June 2006. (a1, b1): Seasonal cycle, (a2, b2): daily-averaged time series at (a) 30°S and (b) at 34°S. Red lines indicate plus/minus one standard deviation. Green lines denote 3-months running means. Units are in 10^6 m^3/s.

gradient through the ITF which results in a weaker LC. The time series shown in Fig. 13 depicts distinct inter-annual signals of top-to-bottom transports in the LC area. This is confirmed by the spectral analysis which reveals additional peaks on seasonal, annual and quasi-biennial time scales (not shown).

Table 3
Depth-integrated transports (0–300 m) of Leeuwin Current System

	Range (Sv;1 Sv = 10^6 m^3/s)	Mean and std. dev. (Sv)
25.8°S, 111.5–113.0°E	+6.9 to −10.0	-1.8 ± 2.3 (-2.9 ± 1.5)
30.0°S, 113.5–115.0°E	+9.0 to −11.8	-2.2 ± 2.9 (-3.6 ± 1.8)
34.0°S, 113.5–115.0°E	+8.8 to −13.4	-3.1 ± 2.6 (-4.1 ± 2.0)

Positive (negative) values indicate northward (southward) transports. Values in parentheses are integrals over southward velocities ("Leeuwin Current") in domain.

3.2.2. The South Australian Current system

In austral summer a high pressure ridge over the Great Australian Bight (GAB) induces a prevailing south-easterly wind field (Fig. 4a). In winter this anticyclone moves to the north resulting in a predominantly westerly wind regime (Fig. 4b). During austral winter a continuous current extends from the LC to the southern tip of Tasmania (Fig. 14b) which does not exist in austral summer (Fig. 14a). The path of the shelf-edge flow off southern Australia was documented in detail by, e.g., Middleton and Cirano (2002), Middleton and Platov (2003), Cirano and Middleton (2004) and Ridgway and Condie (2004). They show that the essentially zonal shelf-edge flow in July along the southern Australian coast arises from a high coastal sea level maintained by onshore Ekman flow driven by winter westerly winds plus a further alongshore pressure gradient. The maximum eastward flow along Australia's southern shelves coincides with the maximum transport of the LC which provides the source water for the South Australian Current (SAC). North of Tasmania the near-surface SAC branches off into two components through Bass Strait and along the west (Zeehan Current) and south-east coasts of Tasmania (Fig. 14b).

The seasonal reversal of coastal wind stresses in the GAB drives onshore Ekman transport and coastal downwelling during austral winter (Fig. 14b) and upwelling favourable conditions in austral summer (Fig. 15a) (Middleton and Cirano, 1999; Cirano and Middleton, 2004). The positive mean wind stress curl in the GAB and related Sverdrup response generates a meandering broad westward flow which is located some 150–200 km from the southern coastal boundary (Fig. 14c and d). This feature is the surface expression of the Flinders Current (FC) which is a year-around upwelling favourable subsurface current, flowing westward

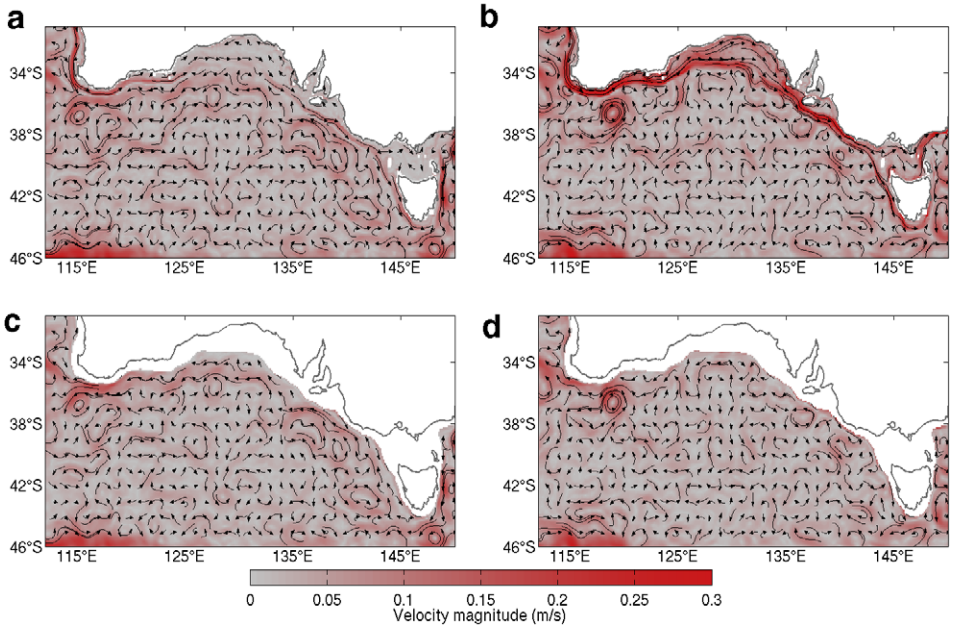

Fig. 14. Seasonal circulation off southern Australia, as in Fig. 11. Every 10th vector is shown. Vector lengths correspond to 30 day Lagrangian trajectories.

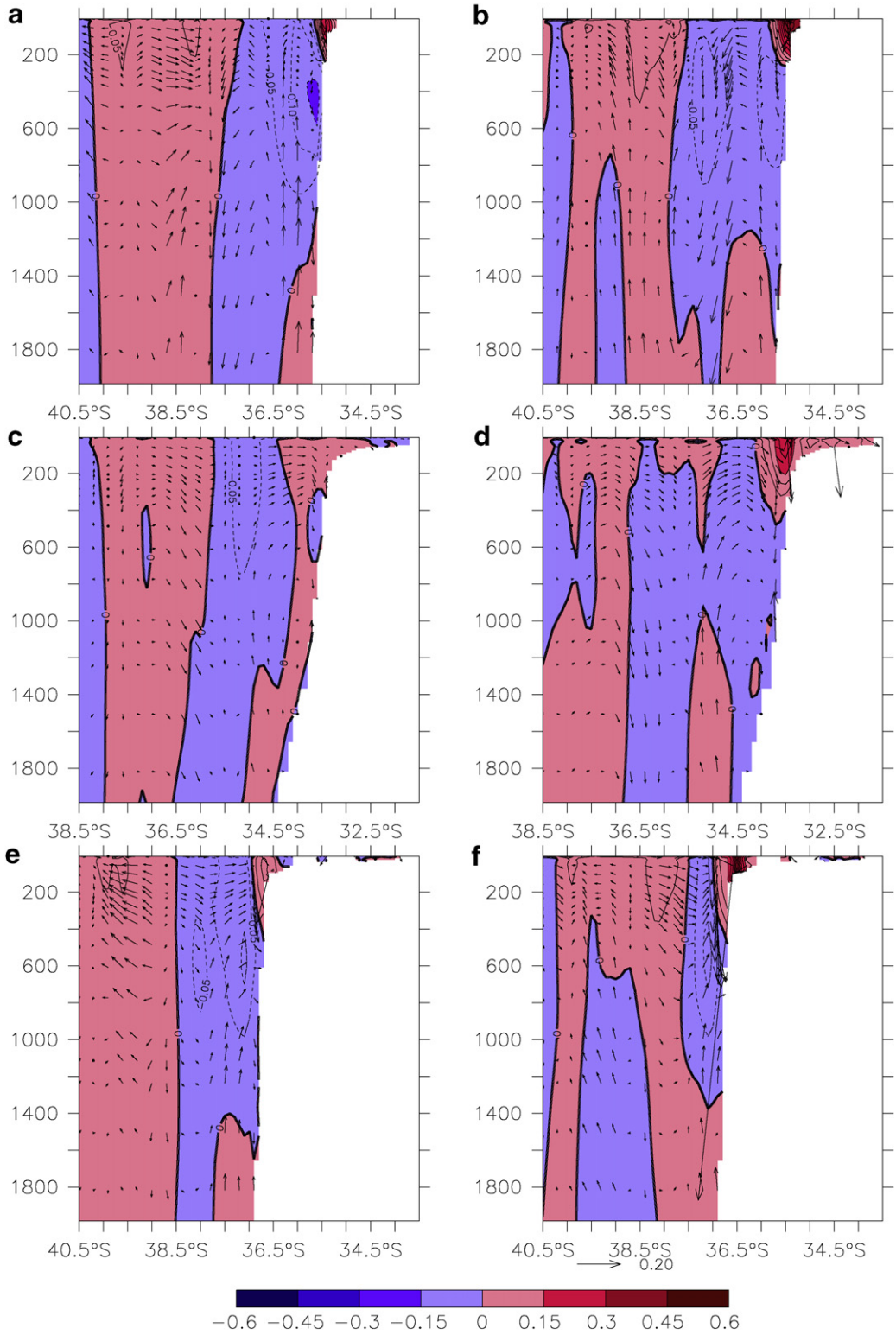

Fig. 15. Seasonal circulation off southern Australia. Notation as in Fig. 11 but for vertical sections at 117.5°E (a, b), 130°E (c, d), and 137°E (e, f). Red (blue) color shows eastward (westward) currents. Circulation in (v, w) plane is superimposed as vectors (w component re-scaled by a factor of 5000). Reference vector is shown underneath (f). See Fig. 5 for geographical location of sections.

along Australia's southern shelves (Middleton and Cirano, 2002; Ridgway and Condie, 2004). The permanent near-coastal westward current with maximum velocities of about 15 cm/s in Fig. 15a–f resembles many of the described features of the FC at various longitudes south of Australia. However, it extends to greater depths (sometimes to the bottom, not shown) than described hitherto.

Fig. 16a shows the seasonal transports of the SAC and FC at 130°E with transports calculated between 31.5°S and 35.0°S over 0–1200 m depth. The positive (negative) curve denotes eastward (westward) transport

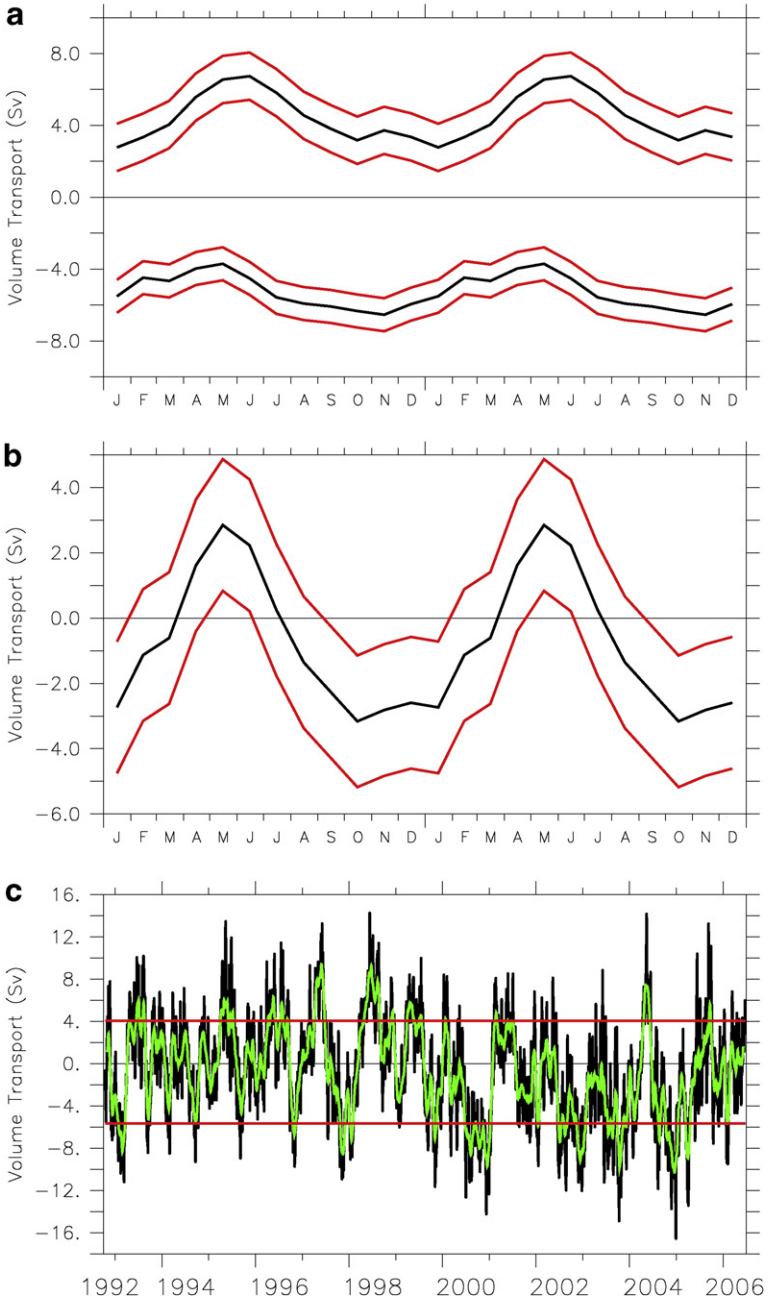

Fig. 16. Transports of South Australian Current system (31.5–35.0°S, 0–1200 m) at 130°E for period October 1992 to June 2006. (a) Upper part: seasonal eastward current (SAC), lower part: seasonal westward current (FC). (b) Seasonal cycle (sum of (a)), and daily-averaged time series of total transport. Red lines indicate plus/minus one standard deviation. Green line denotes 3-months running means. Units are in 10^6 m^3/s.

Table 4
Depth-integrated transports of South Australian Current System

	Range (Sv;1 Sv = 10^6 m^3/s)	Mean and std. dev. (Sv)
117.5°E, 35.0–36.0°S, 0–300 m	+11.3 to −7.8	$+1.2 \pm 2.7$ ($+2.5 \pm 1.7$)
130.0°E, 31.5–35.0°S, 0–1200 m	+14.4 to −16.8	-0.8 ± 4.9 ($+4.5 \pm 2.6$)
137.0°E, 36.0–38.0°S, 0–300 m	+10.7 to −7.0	$+0.8 \pm 2.5$($+2.6 \pm 1.7$)

Positive (negative) values indicate eastward (westward) transports. Values in parentheses are integrals over eastward velocities (“South Australian Current”) in domain.

of the SAC (FC), plus respective standard deviations. The SAC (FC) transport has a maximum (minimum) during April to June and a minimum (maximum) during October to January which is in close agreement with observations (Ridgway and Condie, 2004). Annual mean transports are $+4.5 \pm 2.6$ Sv for the SAC and -5.3 ± 3.2 Sv for the FC. However, we note that the westward velocity field between 31.5°S and 38.0°S yields a total mean transport of the FC of −35 Sv, which suggests that, unlike many previous studies, the whole water columns needs to taken in to account to describe and understand the circulation in the GAB.

At 130°E and between 31.5°S and 35.0°S (0–1200 m) the ocean reanalysis yields a total transport for the South Australian Current system (SAC plus FC) of -0.8 ± 4.9 Sv (Fig. 16b and Table 4). Fig. 16c shows the respective time series. The associated power spectrum of transport variability peaks at annual and quasi-biennial periods with secondary maxima at semi-annual time scales (not shown).

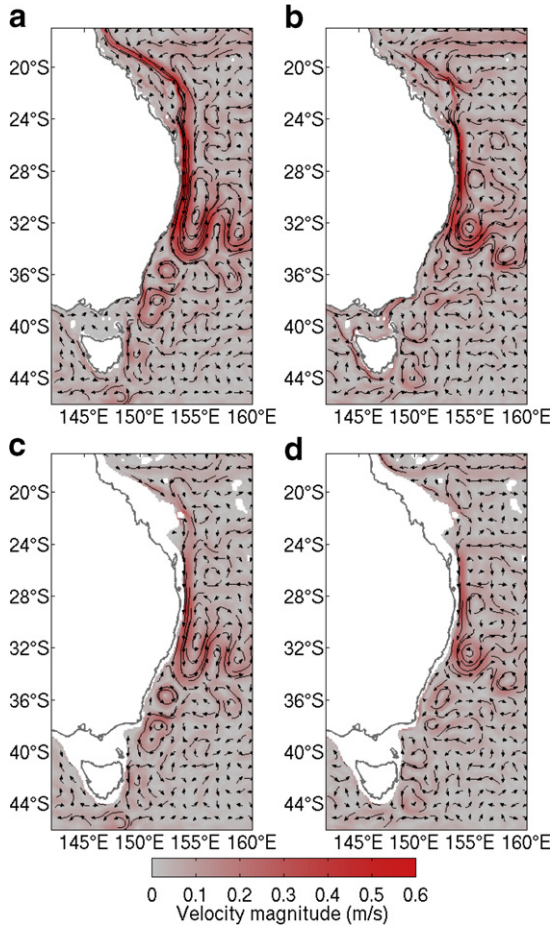

Fig. 17. Seasonal circulation off eastern Australia, as in Fig. 11. Every 10th vector is shown. Vector lengths correspond to 15 day Lagrangian trajectories.

Depending on location and definition the velocity fields and associated transports are in good agreement with model estimates and observations provided by Cirano and Middleton (2004), although our transports (covering a larger depth range) are slightly higher than in their study. Furthermore, the model transport is always to the east at 130°E even when the winds would be expected to produce a westward transport. Part of these discrepancies are associated with the fact that the shelf-edge current system south of Australia is dominated by eddies. Small errors in the thermohaline circulation may overwhelm the wind-forced circulation on the shelves both here and elsewhere. Equally, there might be errors in the local forcing provided by the ECMWF wind stress fields and surfaces fluxes of heat and freshwater. Consequently, it is difficult to construct a simple and coherent picture of the large-scale and time-mean circulation in this area from short observation records. Furthermore, it is difficult to separate the near-surface and thermocline circulation from the deeper circulation. The much weaker velocities in the deep ocean still considerably contribute to total transports in this region.

3.2.3. The East Australian Current system

The East Australian Current (EAC) is the most energetic feature in the subtropical Southwest Pacific region. The EAC is a strong western boundary current flowing southward with vigorous eddy variability (Fig. 6). It is driven by input from the South Equatorial Current (SEC) which bifurcates near 18°S at the continental shelf slope, resulting in two net longshore currents on the slope (Brinkman et al., 2002; Ridgway and Dunn, 2003) (Fig. 17). Its maximum velocities near the surface in both our reanalysis and observations exceed 1 m/s (Roughan and Middleton, 2004) (but are smaller in the monthly averages shown in Fig. 17a and b). Although the core of the EAC is near the surface it often extends to the bottom of the shelf (Fig. 17c and d). Underneath the EAC the northward flowing East Australian Undercurrent (EAUC) can be found (Fig. 18a and b) which is attached to the continental slope. In the reanalysis a weak EAUC exists all year round at 22°S and episodically reaches abyssal depths. Depending on location and season it reaches velocities of up to 0.1 m/s.

The EAC also exhibits a strong retroflection between 33°S and 35°S (Ridgway and Dunn, 2003) (Fig. 17) where it separates from the continental margin and curls back upon itself. The exact location of this partial separation point is likely a function of the zonally integrated regional wind stress curl field (Tilburg et al., 2001).

Once partially separated from the coast the EAC forms a distinct frontal zone (Tasman Front) which separates warm waters from the Coral Sea and cooler waters from the Tasman. The Tasman Front can be found virtually at all depth levels and can be tracked across the Tasman Sea up to and around the northern tip of New Zealand (Tilburg et al., 2001; Ridgway and Dunn, 2003). Instabilities in the retroflection area are the source of predominantly warm-core anticyclonic eddies which propagate southward beyond the partial separation point (Mata et al., 2000; Marchesiello and Middleton, 2000; Mata et al., 2006) while a combination of flow instabilities and upper-ocean-topographic coupling contributes to the formation of meanders in the Tasman Front (Tilburg et al., 2001).

The narrow shelf south of the GBR creates a strong EAC which shows maximum transports between about 25°S and 30°S (Marchesiello and Middleton, 2000). In the reanalysis we find the strongest currents in the retroflection area. In austral summer the monthly averaged EAC reaches about −0.9 m/s at the surface while its retroflected maximum exceeds 0.4 m/s (Fig. 18c). We note that the retroflection zone and the Tasman Front are associated with strong vertical velocities of up to ±20 m/day (Fig. 18c and d).

The southward extension of the EAC reaches as far as Tasmania (Fig. 17c and d). Once it has rounded the southern tip of Tasmania it forms the source water of the FC (Middleton and Cirano, 2005). In Fig. 18e the EAC is seen as a weak southward current in the vicinity of the Tasmanian coast. During austral winter the extension of the SAC, the Zeehan Current, flows northward at this latitude.

The northbound branch of the bifurcated SEC provides the source water of the GBR Shelf Current and the Coral Sea Gyre (Fig. 19). It feeds the quasi-stationary Coral Sea Gyre which is associated with notable transports. The simulated transports are largest in austral winter (Fig. 19b and d) and are mostly barotropic (not shown). Across a section between the Australian coast and 155.5°E (Fig. 19a) this gyre advects 18.9 ± 16.2 Sv but between Papua–New Guinea and 12.5°S the highly variable circulation decreases to 8.2 ± 19.1 Sv (Hiri Current Burrage, 1993). The associated current bifurcates at about 10°S in the Solomon Sea, part of which

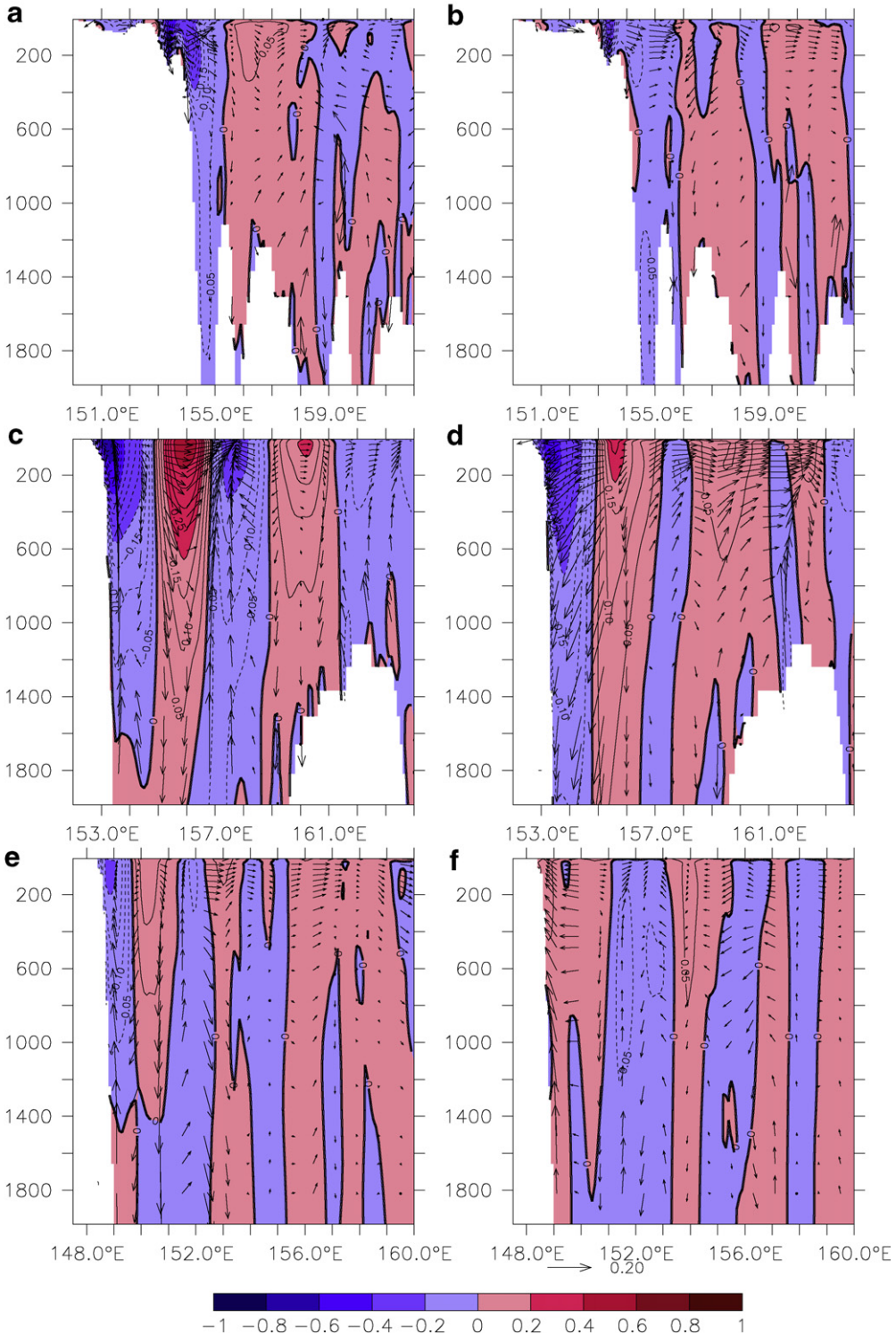

Fig. 18. Seasonal circulation off eastern Australia. Vertical sections at 22°S (a, b), 32°S (c, d), and 42°S (e, f). Notation as in Fig. 12. See Fig. 6 for geographical location of sections.

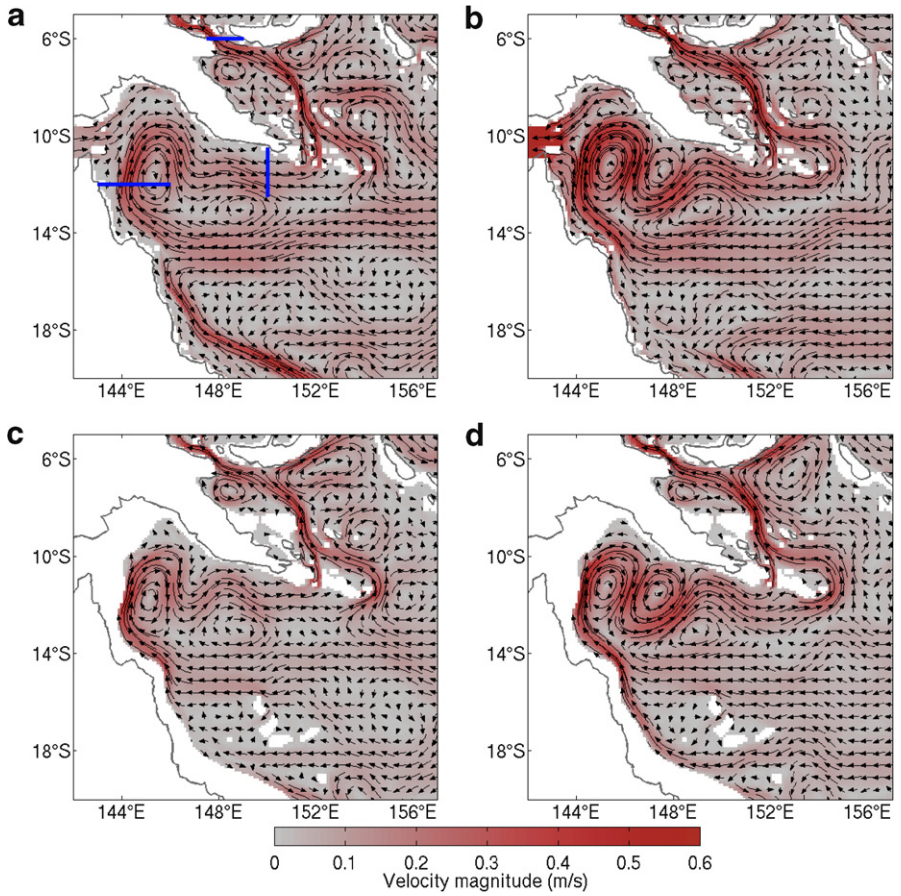

Fig. 19. Seasonal circulation in the Coral Sea, as in Fig. 11. Every 5th vector is shown. Vector lengths correspond to 7 day Lagrangian trajectories. The blue lines in (a) indicate vertical sections discussed in subsequent text.

turns eastward into the South Pacific via Solomon Strait and St. George's Channel. The other part leaves the area through Vitiaz Strait (147–149°E, 6°S) at a rate of 11.1 ± 4.0 Sv and forms part of the Papua–New Guinea Coastal Current.

Torres Strait is a very shallow (20 m) gap between northern Australia (Cape York) and Papua–New Guinea. Even in a 1/10° model with 10 m vertical resolution near the surface the shallow circulation of Torres Strait is not well simulated. We therefore refrain from an investigation of its transport.

We now return to the EAC and its associated transports. In the reanalysis the transport of the EAC is strongly depth-dependent. For instance, at 32°S (Table 5) the mean EAC transports are between 0 and 300 m: -17.4 ± 8.3 Sv, between 0 and 1000 m: -36.8 ± 18.5 Sv, between 0 and 2000 m: -49.4 ± 26.1 Sv and between 0 and 5000 m: -62.1 ± 34.1 Sv. Although the core of the EAC is located in the upper part of

Table 5
Depth-integrated transports of East Australian Current System

	Range (Sv;1 Sv = 10^6 m^3/s)	Mean and std. dev. (Sv)
22.0°S, 150.0–156.0°E, 0–600 m	+10.4 to −30.5	-8.2 ± 6.7 (-14.4 ± 5.8)
32.0°S, 152.0–155.0°E, 0–1000 m	+60.3 to −86.4	-28.7 ± 23.5 (-36.8 ± 18.5)
42.0°S, 148.0–152.0°E, 0–1000 m	+21.3 to −36.9	-1.9 ± 6.7 (-15.9 ± 7.4)

Positive (negative) values indicate northward (southward) transports. Values in parentheses are integrals over southward velocities (''East Australian Current'') in domain.

the ocean, these numbers suggest that the EAC sometimes extends to the bottom and proper transport estimates need to take into account deep contributions to the EAC transports as found in other western boundary currents.

The EAC current system has a well-defined seasonal cycle with stronger southward transports during austral summer (Fig. 20a and b). Based on observations, Ridgway and Dunn (2003) provided an estimate of the

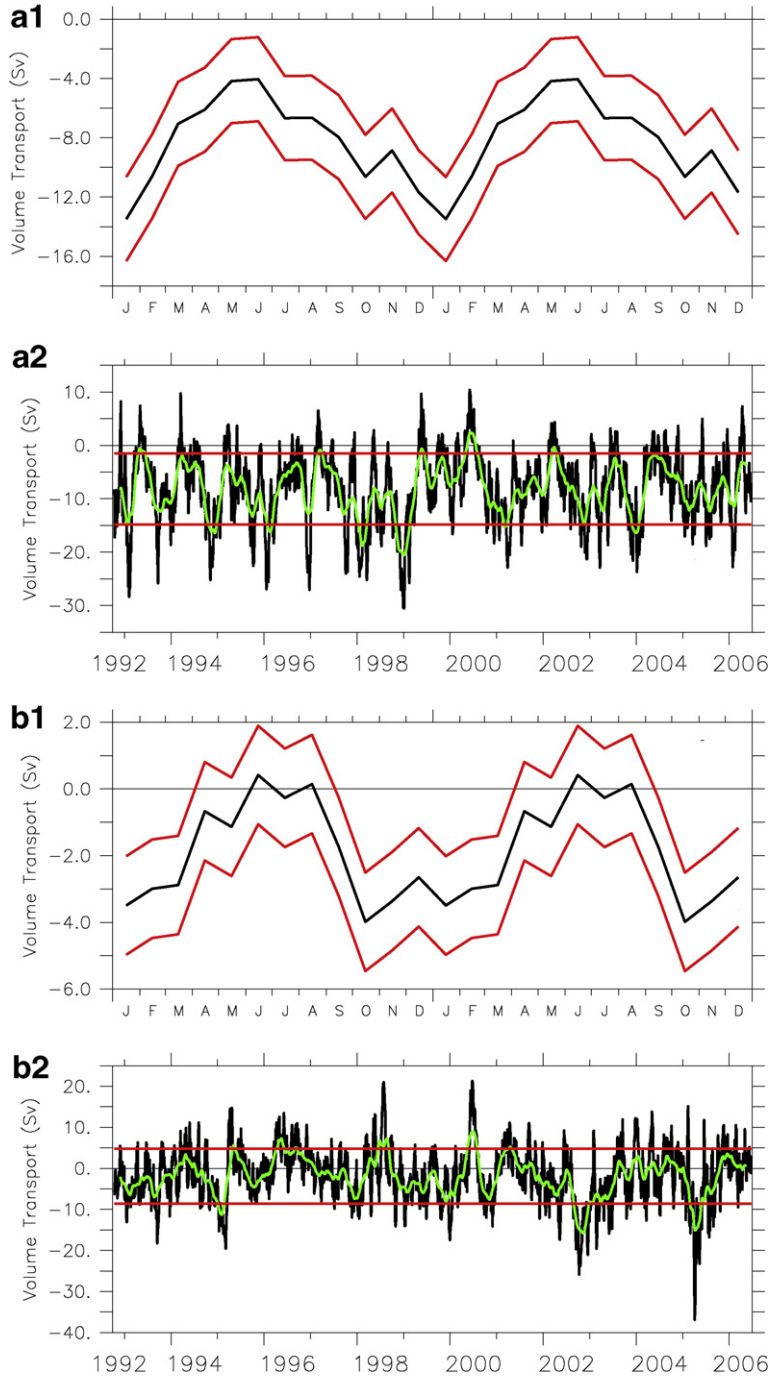

Fig. 20. Total transports of East Australian Current system for period October 1992 to June 2005 at (a) 22°S (0–600 m, 150° E to 156°E) and at (b) 42°S (0–1000 m, 148°E to 152°E). Notation as in Fig. 13.

climatological and geostrophic EAC volume transport (0/2000 db) at 33°S of −37.0 Sv which is 25% less than our estimate of -49.4 ± 26.1 Sv at 32°S.

These results can be compared to other observation-based estimates of the EAC. Using historical oceanographic data, Ridgway and Godfrey (1997) found EAC poleward transports relative to 2000 db at 28°S and between the coast and 155.7°E ranging from 27.4 (austral winter) to 36.3 Sv (austral summer). Chiswell et al. (1997) estimated the flow of the EAC relative to 2000 db and between the coastline and 154.8°E at 29°S, using CTD data gathered over five cruises between 1990 and 1994 to be between −22.2 and −42.2 Sv.

Based on a 23-months long deployment (1991–1993) of a mooring array, Mata et al. (2000) provide an observed mean volume transport at 30°S and between the coast and 154.4°E of 22.1 ± 30 Sv. Their measurements show the EAC as a narrow, swift, and highly variable current centered at 40 km from the coast with strong shear in the upper 1000 m and mean southward velocities of 0.6 m/s in the core. The measurements also revealed a thick countercurrent underneath the poleward flow. Occasional intense northward flow events were observed where total transports reached up to 50 Sv northward. On those occasions the southward boundary current changed from being surface-intensified and mainly baroclinic to northward and more barotropic, related to the northward migration of the EAC coastal separation point. The model reproduces these peaks in observed transport fluctuations as shown in Fig. 20 and as documented by the standard deviation shown in Table 5. For example, at 32°S simulated transports between 0 and 1000 m range from +60.3 to −86.4 Sv.

According to Ridgway and Godfrey (1997) as much as 1/3 of the original EAC continues its path as isolated eddies beyond the partial separation point towards Tasmania. They estimated the strength of the geostrophic (0/2000 db) Tasman Sea outflow at 44°S to be 7.1 Sv. In the reanalysis about 25% of the southward transport at 32°S (36.8 Sv) flows around the southern tip of Tasmania (9.3 Sv). Based on a high-resolution regional model, Cirano and Middleton (2004) estimated the magnitude of the Tasman outflow. In their model the outflow varies in magnitude on an interannual time scale between −5 and 21 Sv.

In summary, the time-mean and seasonal EAC transports are influenced by strong temporal variability associated with dominant eddy fields; the associated volume transports can reach values which are significantly larger than the mean flow of the EAC (Roughan and Middleton, 2004). The total (barotropic plus baroclinic) transport estimates from our reanalysis are at the upper end of the predominantly geostrophic estimates based on observations.

The time series of the EAC current system at 22°S and 42°S (Fig. 20) show responses on seasonal, annual and interannual time-scales. Mata et al. (2000) and Bowen et al. (2005) showed that the variability of southwestward propagating eddies at 30°S has spectral peaks between 90 and 180 days. These spectral peaks are reproduced by the model (not shown).

4. Conclusions

The dynamics of an eddy-dominated turbulent flow are essentially nonlinear and unstable. To obtain reliable three-dimensional flow estimates one needs to combine observations with an eddy-resolving OGCM based on primitive equations. The former is needed to constrain the model, the latter is needed to dynamically interpolate observations in data sparse regions. Here, we have examined regional details of the circulation of the ITF and around Australia in an ocean circulation reanalysis effort.

The primary advantage of this study over previous regional model investigations is the initialization of our model with observations. This approach guarantees that, within prescribed error margins, the model's thermodynamics and dynamics is in close agreement with observations. Secondly, as our model is of global scale, we avoid problems with open boundary conditions.

The eddy-resolving resolution of our reanalysis has provided new insights in well-known features of the regional circulation as well as identified several previously unrecognized aspects of the regional flow patterns. The reanalysis also provides a new source of information for further studying the circulation in the Asian–Australian region.

The key findings of this study are:

– Total volume transport through the ITF in the reanalysis is -9.7 ± 4.4 Sv and is 33% less than transports based on Godfrey's Island rule (Qu et al., 2005: −14.6 Sv) but consistent with recent estimates of about

10 Sv (CLIVAR-GOOS Indian Ocean Panel and collaborators, 2005). However, if one takes into account differences in the forcing fields (ERA-40 vs. operational ECMWF product) the agreement with observations improves in the more recent model years 2002–2006 (-12.5 ± 3.9) compared to previous model years 1992–2005 (-8.4 ± 4.1 Sv).

- The relatively high spatial resolution of the model also allows for a realistic simulation of transports and its variability through major straits of the archipelago. For example, Susanto and Gordon (2005) quote a total depth-integrated transport of $(-)8.1 \pm 1.5$ Sv from a 20-month-long mooring in Makassar Strait in the late 1990s, which supports the results from our reanalysis (-8.4 ± 3.8 Sv).
- Due to the impact of eddies on boundary currents associated transport variability in the LC, SAC and EAC generally represents a large proportion of total transports. This is also confirmed by inspection of Fig. 7 which shows that eddy kinetic energy contributes about 50% to total kinetic energy in these currents.
- A surprising result, which contradicts some earlier findings, is the vertical extent and depth-dependence of major Australian boundary currents, particularly the SAC and EAC. For instance, the depth-integrated transport of the EAC at 32°S (Table 5) between 0 and 300 m is -17.4 ± 8.3 Sv, between 0 and 1000 m it is -36.8 ± 18.5 Sv, between 0 and 2000 m it is -49.4 ± 26.1 Sv and between surface and bottom it is -62.1 ± 34.1 Sv. Although the core of the EAC is located in the upper part of the ocean, these numbers suggest that in order to obtain accurate transport estimates future modelling as well as observational programs should take into account the whole water deep column.

However, due to the relatively short integration period of 14 years imprints of individual eddies on the long-term mean circulation are to be expected in some locations. We will verify this in the future as we repeat our reanalysis over a longer period of time. Use of reconstructed altimetric data sets (e.g., Church and White, 2006) prior to 1992 offers an opportunity to significantly extend reanalyses of the kind presented in this study. Ongoing reanalyses efforts will ultimately support the identification of decadal signals in the oceans of the Asian–Australian region.

The reanalysis data set and other eddy-resolving model simulations are available free of charge for registered users (contact: david.griffin@csiro.au).

Acknowledgments

This publication is a contribution to the project Bluelink – Ocean Forecasting Australia, which is co-funded by the Australian Bureau of Meteorology, the Royal Australian Navy and the Commonwealth Scientific and Industrial Research Organisation. We especially acknowledge the numerous researchers who have contributed to this project through providing their observational data sets. Susan Wijffels, George Cresswell, Detlef Quadfasel and John Middleton plus two anonymous reviewers provided helpful comments on an earlier draft of this manuscript. Drifter data were provided by the Drifting Buoy Data Acquisition Centre. Some plots were created with the FERRET plot software package (http://www.pmel.noaa.gov).

Appendix. Observations and data assimilation

A complete description of the Bluelink Ocean Data Assimilation System (BODAS) is presented by Oke et al. (2005) and a comprehensive evaluation is contained in Oke et al. (2008a). Briefly, BODAS is a sequential data assimilation system that uses multivariate Ensemble Optimal Interpolation (EnOI; Oke et al., 2002). EnOI is a simplified version of the Ensemble Kalman Filter (Evensen, 2003) based on a stationary ensemble of modelled anomalies of all prognostic variables (T, S, and sea-level) to approximate Forecast Error Covariances (FECs). BODAS uses a 72-member ensemble of intraseasonal model anomalies computed from a 9-year spin-up run. The FECs are localised around each observation with an isotropic quasi-Gaussian function, after Houtekamer and Mitchell (2002). This localisation reduces the FECs to exactly zero over a distance of 8° from each observation. The FECs are intended to reflect the length-scales and the anisotropy of the ocean circulation in different regions (Oke et al., 2008a). Both the FECs and the data assimilation itself use observations of temperature, salinity and satellite-derived along-track sea-level anomalies (SLA).

Throughout BRAN, BODAS assimilates these observations using a seven-day assimilation cycle. Specifically, we integrate OFAM for 7 days. We then compare the latest daily mean fields from OFAM with observations that fall within a time window of plus or minus 0, 3, 5 days of the current model time for SST, Argo, and altimetry respectively, and compute an analysis. We then nudge OFAM T, S and sea-level towards the analysis for 1 day and then run OFAM for the next cycle. The nudging time-scale is the maximum of the local inertial period and one day. This choice of nudging time-scale means that equatorwards of about 30°S the nudging time-scale is 1 day; and that this time-scale smoothly decreases towards the pole, to a minimum of about 12 h at the edges of the model domain. Based on a limited number of sensitivity experiments, this strategy for initialising the model seems to be reasonable, since it allows the model to internally adjust to the somewhat unbalanced fields. For a more detailed description of this initialisation procedure the reader is referred to Oke et al. (2008a). BODAS assimilates observations from a range of different sources. SLA observations are obtained from all available satellite altimeters (ERS, GFO, Topex/Poseidon, Envisat and Jason) and from 57 coastal tide gauges around Australia. *In situ* temperature and salinity observations are obtained from Argo floats, from the Tropical Atmosphere–Ocean (TAO) array, and from CTD and XBT (temperature only) surveys from a variety of different field surveys, including WOCE, Indian Ocean Thermal Archive (IOTA) and others. The XBT and CTD profiles (excluding Argo) are sourced from the Bluelink Ocean Archive, a quality-controlled data set used to construct CARS2000 (CSIRO Atlas of Regional Seas; Ridgway et al., 2002). SST observations are obtained from Pathfinder for the period 1992–2002; and from AMSR-E satellites for the period 2002–2006.

BODAS requires explicit estimates of observation errors. SLA errors are assumed to be between 4 and 6 cm, depending on the satellite. *In situ* temperature and salinity errors are attributed to a constant instrument error (0.01 °C and 0.05 psu for CTD; 0.2 °C for XBT). SST errors are assumed to be 0.5° for Pathfinder SST and 0.25° for AMSR-E. In addition to these errors an estimate of the representation error, computed using the method described by Oke and Sakov (2008b), is attributed to each observation. The age of each observation, relative to the analysis time, is also used to proportionally inflate the estimated observation errors. At each assimilation step there are typically 1.0×10^6 and 7×10^5 individual SLA and SST observations, respectively. These are processed to form typically 3×10^4 super-observations (i.e. observations representative of a particular water volume) with a spatial distribution that reflects the model grid resolution, with more super-observations in the high-resolution region of the model. The number of temperature and salinity observations available for each 7-day assimilation step changes significantly over the reanalysis period, with about 1500 (300) temperature (salinity) profiles at the start of BRAN and about 3000 (2500) at the end. In regions where the horizontal resolution of observed hydrographic profiles is greater than that of the model, the number assimilated is restricted so they can be used instead for verification.

References

Bowen, M.M., Wilkin, J.L., Emery, W.J., 2005. Variability and forcing of the East Australian Current. J. Geophys. Res. 110. doi:10.1029/2004JC002,533.

Brinkman, R., Wolanski, E., Deleersnijder, E., Mcallister, F., Skirving, W., 2002. Oceanic inflow from the Coral Sea into the Great Barrier Reef. Estuar. Coast. Shelf Sci. 54, 655–668.

Burrage, D.M., 1993. Coral Seas currents. Corella 17, 135–145.

Chassignet, E.P., Verron, J., 2006. Ocean Weather Forecasting: An Integrated View of Oceanography. Springer International Press, 500 pp.

Chen, D., Rothstein, L.M., Busalacchi, A.J., 1994. A hybrid vertical mixing scheme and its application to tropical ocean models. J. Phys. Oceanogr. 24, 2156–2179.

Chiswell, S.M., Toole, J., Church, J., 1997. Transports across the Tasman Sea from WOCE repeat sections: the East Australian Current 1990-94. N. Z. J. Mar. Freshwater Res. 31, 469–475.

Church, J.A., White, N.J., 2006. A 20th century acceleration in global sea-level rise. Geophys. Res. Let. 33. doi:10.1029/2005GL024,826.

Cirano, M., Middleton, J.F., 2004. Aspects of mean wintertime circulation along Australia's southern shelves: numerical studies. J. Phys. Oceanogr. 34, 668–684.

CLIVAR-GOOS Indian Ocean Panel and collaborators, 2005. Understanding the role of the Indian Ocean in the climate system – implementation plan for sustained observations. CLIVAR Project Office, 86 pp.

Domingues, C.M., 2006. Kinematics and heat budget of the Leeuwin Current. Ph.D. Thesis, Flinders University South Australia, 156 p.

Domingues, C.M., Wijffels, S.E., Maltrud, M.E., Church, J.A., Tomczak, M., 2006. Role of eddies in cooling the Leeuwin Current. Geophys. Res. Lett. 33. doi:10.1029/2005GL025,216.

Ducet, N., LeTraon, P.-Y., 2000. Global high-resolution mapping of ocean circulation from TOPEX/Poseidon and ERS-1 and -2. J. Geophys. Res. 105, 19477–19498.
Evensen, G., 2003. The ensemble Kalman filter: theoretical and practical implementation. Ocean Dyn. 53, 343–367.
Fang, F., Morrow, R., 2003. Evolution, movement and decay of warm-core Leeuwin Current eddies. Deep-Sea Res. 50 (Part II), 2245–2261.
Feng, M., Meyers, G., Pearce, A., Wijffels, S., 2003. Annual and interannual variations of the Leeuwin Current at 32°S. J. Geophys. Res. 108. doi:10.1029/2002JC001,763.
Feng, M., Wijffels, S., Godfrey, S., Meyers, G., 2005. Do eddies play a role in the momentum balance of the Leeuwin Current? J. Phys. Oceanogr. 35, 964–975.
Godfrey, J.S., 1989. A Sverdrup model of the depth-integrated flow for the world ocean allowing for island circulations. Geophys. Astrophys. Fluid Dyn. 45, 89–112.
Godfrey, J.S., et al., 1995. The role of the Indian Ocean in the global climate system: recommendations regarding the Global Ocean Observing System. Report of the Global Ocean Observing System Development Panel, Texas A&M University, College Station, TX, USA, 89 pp.
Gordon, A.L., Fine, R.A., 1996. Pathways of water between the Pacific and Indian Oceans in the Indonesian seas. Nature 379, 146–149.
Gordon, A.L., Susanto, R.D., Vranes, K., 2003. Cool Indonesian Throughflow is a consequence of restricted surface layer flow. Nature 425, 824–828.
Griffies, S.M., 2004. Fundamentals of Ocean Climate Models. Princeton University Press, 518 pp.
Griffies, S.M., Hallberg, R.W., 2000. Biharmonic friction with a Smagorinsky-like viscosity for use in large-scale eddy-permitting ocean models. Mon. Weath. Rev. 128, 2935–2946.
Griffies, S.M., Pacanowski, R.C., Rosati, A., 2004. A technical guide to MOM4. GFDL Ocean Group Technical Report No. 5. NOAA/Geophysical Fluid Dynamics Laboratory, 371 pp.
Griffin, D., Wilkin, J.L., Chubb, C.F., Pearce, A.F., Caputi, N., 2000. Oan currents and the larval phase of Australian western rock lobster, *Panulirus cygnus*. Mar. Freshwater Res. 52, 1187–1199.
Haidvogel, D.B., Beckmann, A., 1999. Numerical ocean circulation modelling. In: Environmental Science and Management, vol. 2. Imperial College Press, 318 pp.
Hellerman, S., Rosenstein, M., 1983. Normal monthly wind stress over the world ocean with error estimates. J. Phys. Oceanogr. 13, 1093–1104.
Houtekamer, P.L., Mitchell, H.L., 2002. A sequential ensemble Kalman filter for atmospheric data assimilation. Mon. Weath. Rev. 129, 123–137.
Josey, S.A., Kent, E.C., Taylor, P.K., 1998. The Southampton Oceanography Centre (SOC) ocean – atmosphere heat, momentum and freshwater flux atlas. Southampton Oceanography Centre, Report No. 6, 30 pp.
Kallberg, P., Simmons, A., Uppala, S., Fuentes, M., 2004. The ERA-40 archive, European Centre for Medium-range Weather Forecasts (ECMWF), ECMWF Re-Analysis Project (ERA), ERA-40 Project Report Series 17, 31 pp.
Koblinsky, C.J., Smith, N.R., 2001. Observing the Oceans in the 21st century. GODAE Project Office Melbourne, p. 604.
Leonard, B.P., 1979. A stable and accurate convective modelling procedure based on quadratic upstream interpolation. Comput. Methods Appl. Mech. Eng. 19, 59–98.
Levitus, S., 2001. World Ocean Database, vol. 13. U.S. Department of Commerce. National Oceanic and Atmospheric Administration.
Marchesiello, P., Middleton, J.H., 2000. Modeling the East Australian Current in the Western Tasman Sea. J. Phys. Oceanogr. 30, 2956–2971.
Mata, M., Tomczak, M., Wijffels, S., Church, J.A., 2000. East Australian Current volume transport at 30°S: estimates from the World Ocean Circulation Experiment hydrographic sections PR11/P6 and PCM3 current meter array. J. Geophys. Res. 105, 28509–28526.
Mata, M., Wijffels, S., Church, J.A., Tomczak, M., 2006. Eddy shedding and energy conversions in the East Australian Current. J. Geophys. Res. 111. doi:10.1029/2006JC003,592.
Meyers, G., Bailey, R.J., Worby, A.P., 1995. Geostrophic transport of Indonesian Throughflow. Deep Sea Res. 42, 1163–1174.
Middleton, J.F., Cirano, M., 1999. Wind-forced downwelling slope currents: a numerical study. J. Phys. Oceanogr. 29, 1723–1743.
Middleton, J.F., Cirano, M., 2002. A northern boundary current along Australia's southern shelves: the Flinders Current. J. Geophys. Res. 107. doi:10.1029/2000JC000,701.
Middleton, J.F., Cirano, M., 2005. Wintertime circulation off southeast Australia: strong forcing by the East Australian Current. J. Geophys. Res. 110. doi:10.1029/2004JC002,855.
Middleton, J.F., Platov, G., 2003. The mean summertime circulation along Australia's southern shelves: a numerical study. J. Phys. Oceanogr. 33, 2270–2287.
Molcard, R., Fieux, M., Ilahude, A.G., 1996. The Indo-Pacific Throughflow in the Timor Passage. J. Geophys. Res. 101, 12411–12420.
Morrow, R., Coleman, R., Church, J., Chelton, D., 1994. Surface eddy momentum flux and velocity variances in the Southern Ocean from Geosat altimetry. J. Phys. Oceanogr. 24, 2050–2071.
Oke, P.R., Allen, J.S., Miller, R.N., Egbert, G.D., Koso, P.M., 2002. Assimilation of surface velocity data into a primitive equation coastal ocean model. J. Geophys. Res. 107. doi:10.1029/200JC000511.
Oke, P.R., Schiller, A., Griffin, D.A., Brassington, G.B., 2005. Ensemble data assimilation for an eddy-resolving ocean model of the Australian region. Quart. J. Roy. Meteor. Soc. 131, 3301–3311.
Oke, P.R., Brassington, G.B., Griffin, D.A., Schiller, A., 2008a. The Bluelink ocean data assimilation system (BODAS). Ocean Model. 21, 46–70.
Oke, P.R., Sakov, P., 2008b. Representation error of oceanic observations for data Assimilation. J. Atmos. Oceanic Tech., in press.

Power, S.B., Kleeman, R., Tseitkin, F., Smith, N.R., 2005. BMRC technical report on a global version of the GFDL modular ocean model for ENSO studies. BMRC Report, 18 pp.
Qu, T., Du, Y., Meyers, G., Ishida, A., Wang, D., 2005. Connecting the tropical Pacific with Indian Ocean through South China Sea. Geophys. Res. Lett. 32. doi:10.1029/2005GL024,698.
Ridgway, K.R., Condie, S.A., 2004. The 5500-km-long boundary flow off western and southern Australia. J. Geophys. Res. 109. doi:10.1029/2003JC001,921.
Ridgway, K.R., Dunn, J.R., 2003. Mesoscale structure of the mean East Australian Current system and its relationship with topography. Progr. Oceanogr. 56, 190–222.
Ridgway, K.R., Godfrey, J.S., 1997. Seasonal cycle of the East Australian Current. J. Geophys. Res. 102, 22,921–22,936.
Ridgway, K.R., Dunn, J.R., Wilkin, J.L., 2002. Ocean interpolation by four-dimensional weighted least squares – application to the waters around Australia. J. Ocean Atmos. Tech. 19, 1367–1375.
Roemmich, D., et al., 2001. The global array of profiling floats. In: Koblinsky, C.J., Smith, N.R. (Eds.), Observing the Oceans in the 21st Century, GODAE Project Office Melbourne, p. 604.
Roughan, M., Middleton, J.H., 2004. On the East Australian Current: variability, encroachment, and upwelling. J. Geophys. Res. 109. doi:10.1029/2003JC001,833.
Schiller, A., Godfrey, J., 2003. Indian ocean intraseasonal variability in an ocean general circulation model. J. Climate 16, 21–39.
Schiller, A., Smith, N., 2006. BLUELINK: large-to-coastal-scale operational oceanography in the Southern Hemisphere. In: Chassignet, E.P., Verron, J. (Eds.), Ocean Weather Forecasting: An integrated view of oceanography. Springer International Press, pp. 427–439.
Schiller, A., Wijffels, S.E., Sprintall, J., 2006. Variability of the Indonesian Throughflow: a review and model-to-data comparison. In: Kawahata, H. (Ed.), Global Climate Change and Response of Carbon Cycle in the Equatorial Pacific and Indian Oceans and Adjacent Landmasses. Elsevier Oceanographic Series, pp. 175–210.
Semtner, A.J., Chervin, R.M., 1992. Ocean general circulation from a global eddy resolving model. J. Geophys. Res. 97, 5493–5550.
Sprintall, J., Chong, J., Syamsudin, F., Morawitz, W., Bray, N., Wijffels, S., 1999. Dynamics of the South Java Current in the Indo-Australia basin. Geophys. Res. Lett. 26, 2493–2496.
Sprintall, J. et al., 2004. A new international array to measure the Indonesian Throughflow: INSTANT. EOS 85, 369–384.
Stammer, D., Wunsch, C., Giering, R., Eckert, C., Heimbach, P., Marotzke, J., Adcroft, A., Hill, C.N., Marshall, J., 2003. Volume, heat and freshwater transports of the global ocean circulation 1993–2000, estimated from a general circulation model constrained by World Ocean Circulation Experiment (WOCE) data. J. Geophys. Res. 108. doi:10.1029/2001JC001,115.
Susanto, R.D., Gordon, A.L., 2005. Velocity and transport in Makassar Strait Throughflow. J. Geophys. Res. 110. doi:10.1029/2004JC002,425.
Thompson, R.O.R.Y., 1984. Observations of the Leeuwin Current off Western Australia. J. Phys. Oceanogr. 14, 623–628.
Tilburg, C.E., Hurlburt, H.E., O'Brien, J.J., Shriver, J.F., 2001. The dynamics of the East Australian Current system: the Tasman Front, the Eeast Aukland Current, and the East cape Current. J. Phys. Oceanogr. 31, 2917–2943.
Tomczak, M., Godfrey, J.S., 1994. Regional oceanography: an introduction. Pergamon Press, Oxford.
Wijffels, S., Meyers, G., 2004. An intersection of oceanic waveguides – variability in the Indonesian Throughflow region. J. Phys. Oceanogr. 34, 1232–1253.